

Convective heat and mass exchange at surfaces of horticultural products: a microscale CFD modelling approach

Thijs Defraeye ^{a,*}, Els Herremans ^a, Pieter Verboven ^a, Jan Carmeliet ^{b,c}, Bart Nicolai ^a

^a VCBT / MeBioS, Department of Biosystems, Katholieke Universiteit Leuven, Willem de Croylaan 42, 3001 Heverlee, Belgium

^b Chair of Building Physics, Swiss Federal Institute of Technology Zurich (ETHZ), Wolfgang-Pauli-Strasse 15, 8093 Zürich, Switzerland

^c Laboratory for Building Science and Technology, Swiss Federal Laboratories for Materials Testing and Research (Empa), Überlandstrasse 129, 8600 Dübendorf, Switzerland

Keywords

Convective transfer coefficient; lenticel; droplet; evaporation; apple; computational fluid dynamics

This document is the accepted manuscript version of the following article:

Defraeye, T., Herremans, E., Verboven, P., Carmeliet, J., Nicolai, B. (2012), Convective heat and mass exchange at surfaces of horticultural products: a microscale CFD modelling approach. *Agricultural and Forest Meteorology*, 162-163, 71-84. <https://doi.org/10.1016/j.agrformet.2012.04.010>

This manuscript version is made available under the CC-BY-NC-ND 4.0 license <http://creativecommons.org/licenses/by-nc-nd/4.0/>

* Corresponding author. Tel.: +32 (0)16321618; fax: +32 (0)16322966.

E-mail address: thijs.defraeye@biw.kuleuven.be

Abstract

Knowledge of the convective heat and mass exchange of horticultural products and other plant organs (e.g., leaves) with the environment is of interest for several pre- and postharvest technologies and for plant microclimate analysis. Although these exchange processes often occur at the microscale (e.g. at lenticels, cracks, droplets or stomata, 10^{-4} - 10^{-2} m), they are still often assessed on a macroscale level. In this study, the convective passive scalar (i.e., heat) transfer from a single spherical product is investigated with computational fluid dynamics (CFD). For this purpose, the product is placed in a virtual wind-tunnel environment, thus not in its natural environment, e.g. on a tree. A sphere is used as reference system; an apple fruit is considered as model system. CFD validation is performed for a sphere, indicating a very good performance of the Reynolds-averaged Navier-Stokes shear stress transport $k-\omega$ turbulence model for the drag coefficient, Nusselt number, separation angle and recirculation length over a large Reynolds number range (10 - 3×10^4). These quantities compare well for sphere and apple. The impact of discretely-distributed microscopic scalar sources on the product surface on the convective transfer is analysed by explicitly modelling them. Such sources are representative for moisture loss through lenticels and cracks in the product's cuticle and evaporation of water or pesticide droplets at the surface. As scalar transfer is assumed only to occur locally at these sources, the active surface area is reduced. In this study, it is found that even at rather low surface coverage ratios, relatively large convective flow rates are found, indicating a non-linear dependency on the active surface area. This dependency is a function of coverage ratio, the Reynolds number and the source size. The proposed computational methodology for investigating the effects of these microscopic scalar sources shows a good performance, by which it is a viable alternative for experiments, which are very challenging at such small scales.

1. Introduction

Knowledge of convective heat and mass exchange of plant organs (e.g. fruit, leaves, etc.) with the environment, i.e., via the boundary layer on their surface, is of interest for several pre- and postharvest technologies and for the analysis of the plant microclimate. For horticultural products in particular, these applications include: (1) analysis of product growth (Jones and Higgs, 1982; Lescourret et al., 2001; Saudreau et al., 2007; Majdoubi et al., 2009; Morandi et al., 2010), due to the strong impact of transpiration on transport of water, minerals and nutrients within horticultural products; (2) analysis of water (droplet) evaporation from surfaces of horticultural products, as water availability at the surface determines the degradation risk at lenticels (small openings in the quasi impermeable skin of the fruit, Everett et al., 2008), the cooling potential by mist chilling (Allais et al., 2006) or hydraircooling (Abdul Majeed, 1981), the risk of surface cracking due to water absorption (Sekse, 1995) and the resulting crack contamination by pathogens (Kovacs et al., 1994) or other infections (e.g., apple scab, Leca et al., 2011); (3) analysis of pesticide (droplet) evaporation from fruits or vegetables and leaf surfaces, as pesticide efficiency is dependent on the evaporation rate, thus the droplet lifetime (Boehncke et al., 1990; Yu et al., 2009; Xu et al., 2010): rapid evaporation can result in insufficient droplet spreading, reduced absorption of active chemical components and formation of crystals, whereas slow evaporation may induce germination of pathogens; (4) convective cooling of horticultural products (Alvarez and Flick, 1999; Kondjoyan, 2006; Verboven et al., 2006; Zou et al., 2006; Delele et al., 2009; Ferrua and Singh, 2009; Tutar et al., 2009; da Silva et al., 2010; Dehghannya et al., 2010; Ferrua and Singh, 2011; Martins et al., 2011), to minimise cooling times and to optimise cooler performance; (5) convective drying of horticultural products such as fruit (McMinn and Magee, 1999; Veraverbeke et al., 2003a; 2003b; Kaya et al., 2006; Nguyen et al., 2006; 2007; Lamnatou et al., 2009; Lamnatou et al., 2010; Mujumdar and Law, 2010; Barati and Esfahani, 2011) to optimise processing efficiency, in terms of energy usage and drying time, without compromising the product quality; (6) long-term storage of horticultural products, as storage time, shelf life, quality, weight loss, mould growth risk and postharvest treatment are strongly related to transpiration, respiration and heat transfer (Tashtoush, 2000; Lammertyn et al., 2003a; 2003b; Hoang et al., 2004; Nahor et al., 2005; Kondjoyan, 2006; Acevedo et al., 2007; Ho et al., 2008; Ho et al., 2011), but also to the adsorption of active components (e.g., 1-MCP, Ambaw et al., 2011). Note that these applications cover a

large variety of flow conditions (Reynolds numbers), turbulence levels (laminar vs. turbulent), configurations (stacks vs. single products) and both high and low temperature ranges.

Besides experimental research, the aforementioned applications often rely on numerical modelling to analyse heat and mass transport processes within horticultural products and their (convective) exchange with the environment. In such models, the convective exchange at product surfaces is usually quantified by means of convective heat and mass transfer coefficients, i.e., CHTCs [$\text{Js}^{-1}\text{m}^{-2}\text{K}^{-1}$] and CMTCs [$\text{kgs}^{-1}\text{m}^{-2}\text{Pa}^{-1}$], respectively (Krokida et al., 2002; Kondjoyan, 2006; Datta, 2007a; 2007b). In this study, moisture is considered as the component for mass transfer, but note that also transport of other gasses (O_2 and CO_2) is important for horticultural products, for example for postharvest storage. These convective transfer coefficients (CTCs) relate the convective heat and moisture flux normal to the wall ($q_{c,w}$ [$\text{Js}^{-1}\text{m}^{-2}$] and $g_{v,w}$ [$\text{kgs}^{-1}\text{m}^{-2}$]), i.e., at the air-material interface, to the difference between the wall temperature (T_w [$^{\circ}\text{C}$ or K]) or (partial) vapour pressure at the wall ($p_{v,w}$ [Pa]) and a reference temperature (T_{ref} [$^{\circ}\text{C}$ or K]) or vapour pressure ($p_{v,ref}$ [Pa]), for example the approach flow conditions:

$$\text{CHTC} = \frac{q_{c,w}}{T_w - T_{ref}} \quad (1)$$

$$\text{CMTC} = \frac{g_{c,w}}{p_{v,w} - p_{v,ref}} \quad (2)$$

The fluxes are assumed positive away from the porous material. Note that these transfer coefficients can be determined locally, i.e. at every location on the surface, using local fluxes and surface temperatures or vapour pressures, but they can also be determined for an entire horticultural product, i.e. a bulk transfer coefficient, which is obtained from an averaging procedure over the product surface. A detailed state-of-the art review on CTCs for food, by experiments and numerical modelling, can be found in Kondjoyan (2006). CTCs, however, account for the convective exchange in a quite simplified way: (1) CTCs are often estimated by means of empirical correlations with the free-stream air speed. These correlations were mostly derived for simplified configurations, such as flat plates, cylinders or spheres, which differ to some extent from CTCs of typical horticultural products: these CTCs are strongly dependent on the flow field around the product, which has a

complex dependency on the product shape, the Reynolds number (air speed and product dimension), the orientation of the product towards the approach flow, the turbulence characteristics of the approach flow, the surface roughness of the product and the specific configuration (e.g., products in a stack); (2) The spatial variation of CTCs over the surface is often not accounted for and only an average (bulk) CTC is considered for the product. Consequently, local CTC distributions and heterogeneities are biased; (3) A temporal CTC variation is not accounted for; (4) CMTCs are often estimated from CHTCs by using the heat and mass transfer analogy (Chilton and Colburn, 1934), which only applies under strict conditions (amongst others, no radiation, no coupling between heat and mass transfer, analogous boundary conditions, etc.); (5) CTCs are dependent on the reference conditions (T_{ref} and $p_{v,ref}$), but the location where these are evaluated is often chosen rather arbitrarily for complex flow problems; (6) CTCs are usually determined (experimentally or numerically) by applying homogeneous thermal or mass boundary conditions on the product surface (e.g., temperature), where often a uniform distribution is applied, i.e., a constant value for the entire surface. In reality, however, heterogeneous (thus non-uniform) boundary conditions on the product surface can also occur, for example at discretely-distributed lenticels or surface cracks, as the majority of the transpiration through the cuticle occurs here (Dietz et al., 1988; Veraverbeke et al., 2003a), or for water (or pesticide) droplets. Such specific boundary conditions are not accounted for by conventional CTCs, although the relevant exchange processes actually occur at the microscale (10^{-4} - 10^{-2} m). For leaves, similar conditions are found for stomata, i.e., local elliptical perforations in the epidermis, via which the majority of the leaf's moisture loss occurs.

Due to the aforementioned simplifications, the use of CTCs can seriously compromise the accuracy of convective heat and mass transfer predictions in biosystems engineering applications. This paper aims to alleviate some of the aforementioned limitations regarding CTCs for horticultural products and specifically focuses on providing a better understanding of the influence of heterogeneous scalar boundary conditions, i.e., discretely-distributed microscopic sources (lenticels, cracks, droplets), on these CTCs over a large Reynolds number range. A single horticultural product is considered and heat is taken as the (passive) scalar to study convective transport. The focus is on spherically-shaped objects, as they are representative for many

horticultural products. Since it is rather difficult to obtain high spatial resolution information on the convective transfer (CTCs) over the product's surface experimentally (Kondjoyan, 2006), numerical modelling by means of computational fluid dynamics (CFD) is applied in this study, i.e., by placing the product in a virtual wind-tunnel environment. For this type of convective transfer studies, CFD was already shown to be a valuable alternative (e.g., Defraeye et al., 2010a) and also provides very detailed flow field information. First, the numerical model and simulation method are described. Afterwards, CFD validation is performed for a single sphere. Furthermore, the drag and scalar transfer from a sphere and a typical horticultural product (i.e., an apple fruit) are compared, as a function of the Reynolds number, including the spatial CTC variation over the surface. In addition, the impact of discretely-distributed microscopic scalar sources on the CTC is investigated, with respect to the size of the sources, coverage ratio and Reynolds number.

2. Methods

2.1. Numerical model

Two configurations are considered: (1) a sphere, since its shape is similar to several horticultural products (e.g., apple, tomato, cherry, peach, several berries, etc.), where CTC correlations for spheres are readily available in literature. Note that the aforementioned simplifications (see section 1) apply to these empirical CTCs; (2) an apple fruit, since it is a typical horticultural product which contains lenticels and surface cracks and since water (rain) or pesticide droplets can be found on its surface. The 3D geometrical shape of the apple was obtained from X-ray computed tomography and was smoothed out slightly at the calyx and at the petiole for CFD meshing purposes. The inner structure of the apple, and the heat and mass transport therein, is not modelled since the focus was on air-side transfer (CTCs). The diameter of the sphere (D) is 75 mm and the equivalent sphere diameter of the apple is 76 mm ($D = 2(3V/(4\pi))^{1/3}$, where V is the total volume of the apple). Based on symmetry, the computational model of the sphere is reduced with a factor 4. The computational domains are presented in Figure 1. The blockage ratio, which is the ratio of the frontal area of the sphere/apple to the surface area of the inlet of the computational domain, is 0.6% for the sphere and 0.8% for the apple,

which is sufficiently low (e.g. $< 3\%$, Franke et al., 2007). The domain dimensions and the computational grids are based on best practice guidelines (Casey and Wintergerste, 2000), on the recent single-sphere CFD study of Dixon et al. (2011) and on domain-size and grid sensitivity analysis performed by the authors. Both grids are hybrid grids (hexahedral and prismatic cells) and consist of 2.8×10^6 and 14.3×10^6 cells for the sphere and apple, respectively. Both grids are shown in Figure 2. The spatial discretisation error is estimated by means of Richardson extrapolation (Roache, 1994; Franke et al., 2007), and is about 1% for both drag force and CHTC.

In order to model discretely-distributed microscopic scalar sources on the product surface (representative for e.g., lenticels or droplets, see section 3.3), very small triangular computational cells with a quasi uniform size were used on this surface. Note that, regarding modelling of droplets, only their surface area was considered in this study, and not their thickness (volume), to reduce the complexity of the computational model. The surface area of a lenticel of an apple is about 10^{-7} m^2 (Veraverbeke et al., 2003a); the droplet size (diameter d) of orchard sprays is about $10^{-4} \text{ m} - 10^{-3} \text{ m}$ (Cross et al., 2001; Ebert and Downer, 2006; Melese Endalew et al., 2010), resulting in an equivalent surface area of about $0.1 - 10 \times 10^{-7} \text{ m}^2$. Note that much larger droplets can be found for rain. Based on these data, a representative average surface area of the triangular computational cells (i.e., representing the microscopic scalar sources) is chosen, namely $1.08 \times 10^{-7} \text{ m}^2$, where the standard deviation over the surface is 7%. The corresponding (average) hydraulic diameter of these cells is $2.9 \times 10^{-4} \text{ m}$, which is calculated for comparison with the size of a circular droplet or lenticel on the surface. The hydraulic diameter is defined as four times the cross-sectional area of the cell, divided by its perimeter. The small scale of these surface cells is the main reason for the high number of computational cells in the computational models (2.1×10^5 surface cells on $\frac{1}{4}$ sphere, 8.7×10^5 surface cells on entire apple). Another reason for the high number of cells is the way in which the flow in the boundary layer is modelled: instead of wall functions, which model the flow quantities in the boundary-layer region by calculating them by means of semi-empirical functions (Launder and Spalding, 1974), low Reynolds number modelling (LRNM) is applied, which explicitly resolves the transport in the boundary layer. At high Reynolds numbers, grids constructed to be employed with LRNM of the boundary layer, however, require a high grid resolution (cell density) in the wall-normal direction: the y^+ value in the wall-adjacent cell centre point P (y_P^+) should be about 1, which is

much smaller compared to the requirements for wall functions ($30 < y_P^+ < 500$). Here, y_P^+ is defined as $(\tau_w/\rho)^{1/2}y_P/\nu$, where y_P ($\approx 2.5 \times 10^{-5}$ m in this study) is the distance (normal) from the cell centre point P of the wall-adjacent cell to the wall [m], ρ is the air density (its value in this study was prescribed to be 1.225 kg m^{-3} , i.e. also for the simulations), ν is the kinematic viscosity of air (its value in this study was prescribed to be $1.461 \times 10^{-5} \text{ m}^2 \text{ s}^{-1}$) and τ_w is the shear stress at the wall [Pa], which increases with the Reynolds number. In this study, the highest y_P^+ values are below 1 for all evaluated air speeds. Note that all air properties are assumed constant, where the thermal conductivity of air (λ) in this study was prescribed to be $0.0242 \text{ W m}^{-1} \text{ K}^{-1}$.

At the inlet of the domain, a uniform, low-turbulent velocity is imposed (see Figure 1). Free-stream air speeds (U_{ref}) of 0.002 - 6.325 ms^{-1} are evaluated, resulting in Reynolds numbers of 10 to 3.2×10^4 ($Re = U_{ref}D/\nu$). The turbulence intensity (TI_{ref}) at the inlet is taken 0.1%, which is low and typical for most low-turbulence wind tunnels. The specific dissipation rate (ω [s^{-1}]) is determined from $\omega = k^{1/2}/(0.07C_\mu^{1/4}L)$ (Fluent 12, 2009), where k is the turbulent kinetic energy [$\text{m}^2 \text{ s}^{-2}$], $C_\mu = 0.09$ and L is a length scale which is taken small (arbitrarily) and equal to $D/10$ [m]. The effect of turbulence inlet properties has been a subject of research (Ghisalberti and Kondjoyan, 1999; Peyrin and Kondjoyan, 2002; Kondjoyan, 2006), but an analysis of the impact of these variables was, although feasible, outside of the scope of the present study. Zero static pressure is imposed at the outlet, which is often used in similar studies (e.g., Dixon et al., 2011) and is advised in best practice guidelines (e.g., Franke et al., 2007). Symmetry boundary conditions (slip walls) are used for the lateral boundaries which assume that the normal velocity component and the normal gradients at the boundary are zero. The sphere and apple surfaces are modelled as no-slip walls with zero roughness since surface roughness values cannot be specified if LRNM is used (Fluent 12, 2009).

Heat is taken as the (passive) scalar to study convective transport instead of mass (or combined heat and mass), implying, amongst others, no dependency of air density on the temperature. The reason for this is that the computational cost to evaluate different scalar boundary conditions (see section 3.3) decreased significantly when only heat transfer was accounted for: as the air properties were not taken as a function of temperature, only the scalar field had to be recalculated if different thermal boundary conditions were

imposed at a certain Reynolds number, and not the entire air flow field. Consequently, different scalar boundary conditions could be evaluated more quickly. For mass transfer on the other hand, the air properties (thus air flow) are inherently a function of the mass fraction in the air and of the temperature (e.g., saturation vapour pressure at the surface), although their temperature dependency can be rather limited. Note that heat and mass transport behave quasi analogous under specific conditions (amongst others, similar boundary conditions, no radiation, no coupling between heat and mass transfer which implies low evaporation rates, etc.). Under these conditions, which are often quasi fulfilled for the cases relevant for this study, the heat and mass transfer analogy can be applied to estimate CMTCs out of CHTC data (e.g., see Defraeye et al., 2012). The findings for heat transfer (CHTC) of this study can thus be easily transposed to mass transfer (CMTC).

A temperature of 10°C (T_{ref}) is imposed at the inlet of the computational domain. A uniform temperature (T_w) of 20°C is imposed at the sphere/apple surface. This type of boundary condition (constant/uniform scalar value) was chosen in this study since it is mostly used in literature (see Dhole et al., 2006), compared to the constant flux condition, e.g., to determine correlations of CHTCs with the wind speed for spheres. Consequently, the results of this study can be compared with several other studies and correlations (e.g., see section 3.1). For the simulations with heterogeneous boundary conditions (discretely-distributed scalar sources), a different type of thermal boundary condition is imposed: a constant temperature (20°C) is only imposed at discrete locations (computational cells) on the sphere/apple surface and the rest of the surface is assumed impermeable for heat (no-flux condition), i.e. adiabatic, thus for this part of the surface a zero wall-normal temperature gradient is present in the wall-adjacent cells. This specific boundary condition is implemented by means of a user-defined function in the CFD code. This boundary condition, i.e., including discretely-distributed scalar sources, is more representative for convective mass exchange at droplets on the surface or at lenticels or surface cracks, compared to a constant scalar value imposed uniformly over the entire sphere/apple surface: at these parts of the surface, a constant scalar value (e.g., temperature) is found and scalar transfer can occur, whereas quasi no scalar transfer from/to the surface is possible in the other parts. Note that this particular type of boundary condition showed quite slow convergence behaviour with respect to the scalar, where the scalar convergence speed decreased with decreasing coverage ratio. This slow

Defraeye T., Herremans E., Verboven P., Carmeliet J., Nicolai B. (2012), Convective heat and mass exchange at surfaces of horticultural products: a microscale CFD modelling approach, *Agricultural and Forest Meteorology* 162-163, 71-84. <http://dx.doi.org/10.1016/j.agrformet.2012.04.010>
<http://www.journals.elsevier.com/agricultural-and-forest-meteorology/>

convergence behaviour is probably related to the very small size of the scalar sources, which are distributed heterogeneously over the surface.

2.2. Numerical simulation

The simulations are performed with the CFD code ANSYS Fluent 12, which uses the control volume method (using Cartesian coordinates). General information on the numerical methods used to discretise and solve the transport equations in CFD can be found in Ferziger and Peric (2002), amongst others. In the past, CFD has been extensively applied to model fluid flow around a single sphere (Johnson and Patel, 1999; Feng and Michaelides, 2000; Constantinescu and Squires, 2004; Dhole et al., 2006), in stacks of spheres (Augier et al., 2010) but also for several food processing applications (Verboven et al., 1997; Hu and Sun, 2001; Verboven et al., 2003; Delele et al., 2008). The accuracy of CFD simulations depends to a large extent on the turbulence-modelling and boundary-layer modelling approaches that are used, which has to be quantified by means of validation experiments/simulations. For such validation, often drag coefficients, Nusselt numbers, separation angles or recirculation lengths from CFD are compared with available experimental data, e.g., of spheres, cylinders or stacks of spheres.

Regarding flow around a single sphere, Dixon et al. (2011) recently evaluated the accuracy of several turbulence modelling approaches. Note that they applied a uniform (homogeneous) boundary condition at the surface, whereas in the present study also the influence of heterogeneous boundary conditions (microscopic scalar sources) was evaluated. They concluded that steady Reynolds-averaged Navier-Stokes (RANS) in combination with the shear stress transport $k-\omega$ model (SST $k-\omega$, Menter, 1994) was sufficiently accurate for convective heat transfer predictions, but for drag predictions, it was only acceptable as an engineering approximation. Large-eddy simulation (LES) provided more accurate results regarding drag but at a much higher computational cost. Moreover, LES requires very detailed knowledge of the inlet conditions (see review by Kondjoyan, 2006), which are generally not known by food engineers. Due to the restrictions of LES, RANS is often considered as the only practical alternative to model large complex systems, such as flow

in stacks of horticultural products. Therefore, steady RANS is also used in this study, together with the SST k- ω model, as implemented in ANSYS Fluent 12 (Fluent 12, 2009). Note that unsteady RANS (URANS) was not evaluated in this study, due to the higher computational time and since previous studies (Constantinescu et al., 2003; Dixon et al., 2011) did not indicate an increased accuracy compared to RANS. LRNM (assuming zero wall roughness, see section 2.1) is applied to resolve the transport in the boundary-layer region. LRNM is actually included in the SST k- ω model (Fluent 12, 2009), i.e. the SST k- ω model is used as a LRNM model and does not require damping functions in the vicinity of the wall. LRNM however requires a very fine grid in the near-wall region, in contrast to wall functions. This grid requirement increases the computational cost of the (RANS) simulation significantly, by which LRNM is often not used or not practically applicable for complex 3-D configurations (Kondjoyan, 2006). The accuracy of the (LRNM) SST k- ω model is evaluated in detail in section 3.1 by means of a validation study for a sphere, by comparison with experimental data (drag coefficient, bulk convective heat transfer coefficient, etc.) from literature.

Furthermore, second-order discretisation schemes are used throughout. The SIMPLE algorithm is used for pressure-velocity coupling. Pressure interpolation is second order. Buoyancy effects are not taken into account in the simulations since the focus of this paper is on passive scalar transport. In this case, the flow field is independent of the imposed scalar (thermal) boundary conditions, which implies forced convective flow and passive scalar (heat) transfer. Thereby, the reported results are more generally useable, i.e., they are also applicable for transport of other scalars, such as water vapour. Note that not accounting for buoyancy in the simulations also allowed to specify larger temperature differences between the product surface and the air flow, which avoids numerical round-off errors related to very small temperature differences. Radiation is also not considered in the simulations, amongst others since the heat and mass transfer analogy is not valid if radiation is accounted for. Iterative convergence of the numerical simulation was assessed by monitoring the velocity, turbulent kinetic energy and temperature on specific locations in the flow field, namely where large gradients are found (i.e., in the recirculation zone), and the drag and heat fluxes (surface-averaged values) of the sphere and apple.

3. Results

3.1. CFD validation for a sphere

The accuracy of the SST k- ω model for flow and scalar transfer around a sphere is assessed by comparison with experimental data of different parameters at multiple Reynolds numbers, which are well-established for spheres in several textbooks (e.g., Clift et al., 1978): (1) drag coefficient $C_D = F_d / (0.5 \rho U_{ref}^2 A_f)$, where F_d is the drag force [N] and A_f is the frontal area [m²]; (2) Nusselt number $Nu = CHTC.D/\lambda$; (3) separation angle (θ_s [°]), which is defined as the angle at which the shear stress at the wall is quasi equal to zero. This angle is taken zero at the windward stagnation point; (4) recirculation length (L_r [m]), which is defined as the (maximal) downstream distance from the sphere where the streamwise velocity component becomes zero. L_r is represented dimensionless by means of D .

The following empirical functions of C_D (from Clift et al., 1978), Nu (from Whitaker, 1972) and θ_s (from Clift et al., 1978) for flow around a sphere are used for comparison with CFD simulations. For L_r , empirical data reported by Clift et al. (1978) is taken.

$$C_D = \begin{cases} (24 / Re) (1 + 0.1315 Re^{0.82 - 0.05 \log Re}) & \text{for } 0.01 < Re < 20 \\ (24 / Re) (1 + 0.1935 Re^{0.6305}) & \text{for } 20 < Re < 260 \\ 10^{1.6435 - 1.1242 \log Re + 0.1558 (\log Re)^2} & \text{for } 260 < Re < 1500 \\ 10^{-2.4571 + 2.5558 \log Re - 0.9295 (\log Re)^2 + 0.1049 (\log Re)^3} & \text{for } 1500 < Re < 12000 \\ 10^{-1.9181 + 0.637 \log Re - 0.0636 (\log Re)^2} & \text{for } 12000 < Re < 44000 \end{cases} \quad (3)$$

$$Nu = 2 + (0.4 Re^{0.5} + 0.06 Re^{0.667}) Pr^{0.4} \left(\frac{\mu}{\mu_{wall}} \right)^{0.25} \quad (4)$$

$$\theta_s = \begin{cases} 180 - 42.5 [\ln(Re/20)]^{0.438} & \text{for } 20 < Re < 400 \\ 78 + 275 Re^{-0.37} & \text{for } 400 < Re < 300000 \end{cases} \quad (5)$$

where μ and μ_{wall} are the absolute viscosities of the fluid and of the fluid at the wall, respectively ([kgm⁻¹s⁻¹]), which are equal in this study (see section 2.1) as air properties are assumed constant; Pr is the Prandtl number ($= c_p \mu \lambda^{-1}$), with c_p the specific heat capacity of air, taken equal to 1006.43 Jkg⁻¹K⁻¹ in this study. A comparison

of these functions and CFD is presented in Figure 3 as a function of the Reynolds number (the data presented in Figure 3 for the apple are discussed in section 3.2). In addition, the local Nusselt number values on the sphere surface are compared in Figure 4 with experimental data of Galloway and Sage (1972), as a function of the angle from the windward stagnation point (θ), within a similar Reynolds number range. Note that a logarithmic scale is used in Figure 3a-b, due to which differences in C_D and Nu will appear less pronounced here. Nevertheless, a very good agreement is obtained for all parameters over the Reynolds number range that is considered in this study (Figure 3), which is quite exceptional for steady RANS simulations. The good performance of the SST k- ω model is most likely related to the fact that it uses a two-equation k- ω model formulation to solve the near-wall region, for which the k- ω model was originally developed, whereas a k- ϵ model formulation is used to solve the turbulent core region of the flow. The SST k- ω model was developed from the standard k- ω model, which often does not perform well in the core region of the flow due to the sensitivity to the imposed free-stream value of ω (Casey and Wintergerste, 2000). The background of the model is explained clearly by Menter (1994). Note that the SST k- ω model also performed well at very low Reynolds numbers, where the flow is essentially laminar. A good agreement with laminar-flow CFD simulations (also included in Figure 3) was thus expected and found, i.e., up to Reynolds numbers of 300 ($U_{ref} = 0.06325 \text{ ms}^{-1}$). At the subsequent (higher) Reynolds number that was evaluated (i.e., $Re = 1000$; $U_{ref} = 0.2 \text{ ms}^{-1}$), laminar flow simulations showed significant discrepancies with the SST k- ω model (e.g., 10% for C_D) as flow became turbulent. Other studies also reported a good performance for drag with the SST k- ω turbulence model for flow around streamlined bluff bodies (amongst others, Defraeye et al., 2010b; Dixon et al., 2011). The agreement of the SST k- ω model for the drag coefficient is, however, significantly better than found by Dixon et al. (2011), of which the data (of their SST k- ω model simulations) are also included in Figure 3a and Figure 3e. In Figure 3e, no logarithmic scaling is used for the drag coefficient to indicate the differences with Dixon et al. (2011) more clearly. The improved accuracy of the present study could be related to the very high spatial grid resolution in the boundary layer, which was applied to model the heterogeneous boundary conditions at the surface (see section 3.3). The agreement with respect to the local Nusselt number distribution (Figure 4) is also satisfactory, based on the limited experimental data for the evaluated Reynolds number range, which was taken similar in Figure 4 for both experimental data and

simulations ($\sim 10^3 - 10^4$). The results of this CFD validation study indicate that the (LRNM) SST k- ω model provides sufficient accuracy to be used for flow and scalar transfer predictions for a single sphere. The performance of the SST k- ω model is assumed to be very similar for flow and scalar transfer around spherically-shaped horticultural products, such as an apple.

3.2 Comparison of sphere and apple fruit

In this section, the C_D , Nusselt number (i.e., representative for the CHTC), L_r and θ_s of a sphere are compared with those of an apple fruit. The aim is to indicate how representative data for spheres are for horticultural products with a similar shape, since such horticultural products are often simplified to spheres in numerical modelling. A comparison of these parameters is presented in Figure 3, as a function of the Reynolds number. L_r of the apple is determined by taking the largest streamwise coordinate of the zero-value isocontour of the streamwise velocity component. Note that the frontal area of the apple, used to calculate C_D , is 5% larger than that of the sphere and that the equivalent sphere diameter of the apple, used to calculate the Nusselt number, is 76 mm. The maximal differences of C_D , Nu , θ_s and L_r between apple and sphere data are below 9%, 6%, 5% and 28%, respectively, where the sphere data agree better with the empirical data. The largest differences between apple and sphere are found at a Reynolds numbers of 10^3 . At this Reynolds number, a highly unstable and irregular wake flow field is found for the apple. This is probably related to the onset of wake instability, which starts at Reynolds numbers between 130 and 400 for a sphere (Clift et al., 1978). Note that RANS is probably not suited to predict a realistic mean flow field in this highly unstable (Reynolds) regime, particularly for asymmetrical geometries such as the apple. Note that the use of unsteady methods (e.g., URANS or LES) could increase accuracy here, however at an increased computational cost and time. For the symmetrical sphere, however, the predicted flow field by RANS seems to be less sensitive here, or, the wake instability occurs at Reynolds numbers somewhere in between the ones evaluated in this study. Thus, in general, a good agreement between sphere and apple fruit is found.

In Figure 5, the distributions of local heat fluxes (normal to the wall) and shear stresses (parallel to the wall) at the wall for both sphere and apple are given as a function of the angle from the windward stagnation point (θ)

for different Reynolds numbers. The local shear stresses are calculated from the product of the absolute viscosity with the wall-normal velocity gradients within the wall-adjacent cells, i.e., between the wall (no-slip condition, zero velocity) and the cell centres of the wall-adjacent cells (wall-parallel velocity). The local heat fluxes are calculated from the product of the thermal conductivity with the wall-normal temperature gradients within the wall-adjacent cells, i.e., between the wall (constant imposed temperature) and the cell centres of the wall-adjacent cells (Fluent 12, 2009). These local shear stresses and heat fluxes are scaled in Figure 5 with the surface-averaged heat flux ($q_{c,w,avg}$) and shear stress ($\tau_{w,avg}$), respectively, which are given in Table 1 for different Reynolds numbers. The average values over one-degree intervals (i.e., sphere segments) are presented. For the apple, a distinct variation of the heat fluxes and shear stresses is present within each of these one-degree intervals, due to the asymmetrical shape of the apple, by which there is some spread on the average value for a specific one-degree interval, particularly at the calyx and petiole. Note that the heat flux is directly proportional to the CHTC (Eq.(1)), due to the imposed constant temperature difference ($T_w - T_{ref}$). A good agreement between apple and sphere data can be observed from Figure 5. The most significant differences appear at angles of about 80°-100°, which is where the calyx and petiole are located. In contrast to quasi-developed flat-plate flow, no distinct correlation between shear stress (skin friction) and heat flux is found. For such flat-plate flow, however, equilibrium conditions are usually fulfilled, i.e., small pressure gradients, local equilibrium between generation and dissipation of turbulent energy and a constant (uniform) shear stress and heat flux in the near-wall region (Casey and Wintergerste, 2000). For the complex 3-D flow fields investigated in this study, such equilibrium conditions are not found, which thus results in a (very) weak correlation between skin friction and scalar transfer (see, amongst others, Launder, 1988; Defraeye et al., 2010a).

The results presented in this section seem to indicate that the flow field and scalar transfer around a sphere are quite representative for an apple with similar dimensions, and thus presumably also for other spherically-shaped horticultural products. Note, however, that the aforementioned CFD data for apple fruit are only based on one specific case (described in section 2.1). Some variation on the data will be introduced by the evaluated species (e.g., apple, avocado, ...), the cultivar (e.g., Jonagold, Gala, ...), the unique shape of each individual

horticultural product, the Reynolds number (air speed and characteristic product dimension), the orientation to the approach flow, the turbulence characteristics of the approach flow, surface roughness of the product and the specific configuration (e.g., horticultural products in a stack).

3.3 Heterogeneous scalar boundary conditions

3.3.1 Background

In this section, a brief background is given on the possible impact of non-uniform (heterogeneous) boundary conditions (i.e., surface coverage) on the resulting convective scalar transfer, compared to homogeneous boundary conditions. CTCs for horticultural products are usually estimated from experiments or numerical simulations on spheres or cylinders where a homogeneous (mostly uniform) scalar boundary condition is imposed at the product surface. In case of such a uniform scalar boundary condition (e.g., constant wall temperature), the CHTC or CMTC (Eqs.(1-2)) can also be written as:

$$\text{CHTC} = \frac{Q_{c,w,avg}}{A(T_w - T_{ref})} \quad (6)$$

$$\text{CMTC} = \frac{G_{c,w,avg}}{A(p_{v,w} - p_{v,ref})} \quad (7)$$

where $Q_{c,w,avg}$ [Js^{-1}] and $G_{c,w,avg}$ [kgs^{-1}] are the surface-averaged heat and mass flows and A [m^2] is the surface area of the body. As mentioned in section 1, such boundary conditions do not match reality in some conditions, amongst others, for droplet evaporation from surfaces of horticultural products or for moisture loss through the cuticle, which often occurs predominantly via the lenticels – small openings in the quasi impermeable skin of the fruit. Here, scalar transfer only occurs at a specific part of the product surface (A_{eff}) instead of at the entire surface (A), namely at discretely-distributed microscopic scalar sources, which implies heterogeneous scalar boundary conditions.

Previous research, however, indicated that the surface-averaged scalar flows ($Q_{c,w,avg}$ or $G_{c,w,avg}$) do not scale linearly with this reduced surface area for scalar transfer (A_{eff} [m^2]), which thereby will have an impact on the

CTCs: Schlünder (1988) showed (analytically) that for laminar boundary-layer flow over a flat surface, under specific conditions, a high mass flow rate could be maintained for a partially-wetted surface, by which the surface behaves actually very similar to a uniformly-wetted surface. These conditions are that the characteristic size of the wetted areas (d [m]) on the surface (called patches, similar to droplets or lenticels in this study) is small compared to the thickness of the viscous sublayer δ_{VSL} (i.e., the lower part of the boundary layer where laminar transport occurs and where large velocity and temperature gradients are found; see, e.g., Defraeye et al., 2010a; [m]), and that the wetted patches are homogeneously distributed along the surface. In such a case, the concentration contours quickly equalise in the lateral direction (become parallel to the wall) further away from these patches (Figure 6a), particularly for small patches. As such, the saturation vapour pressure is found above quasi the entire surface, and not only directly above the wet patches (Schlünder, 1988). Thereby, the surface appears to be quasi completely wet for the flow, i.e. a quasi-uniform vapour pressure is found in horizontal planes within the viscous sublayer, which lies very close to the saturation vapour pressure. This results in a high mass flow rate, even for a reduced wet surface area, i.e., reduced surface saturation (Suzuki and Maeda, 1968; Schlünder, 1988; Belhamri and Fohr, 1996). The analytical expression of Schlünder (1988) is as follows:

$$\frac{G_{c,w,\vartheta}}{G_{c,w,100\%}} = \frac{1}{1 + \Phi} \quad (8)$$

$$\text{with } \Phi = \frac{2}{\pi} \frac{d}{\delta_{VSL}} \sqrt{\frac{\pi}{49}} \left(\sqrt{\frac{\pi}{49}} - 1 \right) \quad (9)$$

where ϑ is the surface coverage ratio ($\vartheta = A_{eff}/A$) and $G_{c,w,\vartheta}$ and $G_{c,w,100\%}$ are the mass flows at the surface (normal to the wall) at a coverage ratio of ϑ and 100%, respectively. This equation is only useable for $\vartheta \leq \pi/4$, since otherwise Φ becomes negative, leading to $G_{c,w,\vartheta} > G_{c,w,100\%}$. Note that Schlünder (1988) assumed only laminar transport in the boundary layer, by which the viscous sublayer thickness (δ_{VSL}) was equal to the entire boundary layer thickness. Schlünder's expression is evaluated in Figure 6b for different d/δ_{VSL} ratios. Low d/δ_{VSL} ratios show relatively high transfer rates, even at very low surface coverage ratios (Schlünder, 1988; Schlünder, 2004). For (turbulent) boundary layers, δ_{VSL} is defined in this study as the region where $y^+ < 5$,

which is approximately the upper y^+ limit of the viscous sublayer (e.g., Cebeci and Bradshaw, 1984). Based on the definition of y^+ , this results in:

$$\delta_{VSL} = \frac{5\nu}{\sqrt{\frac{\tau_w}{\rho}}} \quad (10)$$

δ_{VSL} is thus inversely proportional to the square root of the shear stress at the wall. Note that the shear stress increases with the wind speed (U_{ref}), by which the boundary-layer thickness (thus also δ_{VSL}) will decrease with increasing wind speed. Also note that the principle of the equalisation of the concentration contours (Figure 6a) will be similar for curved surfaces, such as a sphere or an apple, due to the small scales of the microscopic sources.

3.3.2 Thickness of the viscous sublayer

In the remainder of section 3.3, the influence of a reduced surface area for scalar transfer (A_{eff}) will be investigated for spherical objects. The focus will be mainly on a sphere, as a reference system for horticultural products, but apple fruit is also considered as an example. It will be verified how Schlünder's findings for laminar flat-plate flow hold for turbulent flow around spherical objects as in this case δ_{VSL} varies significantly with the angle (from the windward stagnation point). Since the local δ_{VSL} values are to some extent representative for the total turbulent boundary-layer thicknesses, the latter will also vary over the surface. As it is rather difficult to define the total turbulent boundary-layer thicknesses uniformly for complex flow around bluff bodies with recirculation and separation zones, they were not determined in this study. As the scalar transfer from the surface is influenced by the d/δ_{VSL} ratio, a closer look at the δ_{VSL} distribution on the sphere surface is taken. In Figure 7, δ_{VSL} of the sphere (see Eq.(10)) is presented as a function of the angle from the windward stagnation point for several Reynolds numbers. δ_{VSL} is scaled with $\delta_{VSL,avg}$, i.e., the surface-averaged δ_{VSL} over the sphere. The average δ_{VSL} values over one-degree intervals (i.e., sphere segments) are presented. In Figure 8, $\delta_{VSL,avg}$ is compared with the size of the scalar sources (d , hydraulic diameter of triangular computational cells on surface = 2.9×10^{-4} m, representative for, e.g., a lenticel or a droplet) at different

Reynolds numbers by means of the $d/\delta_{VSL,avg}$ ratio. Note that both a normal and a logarithmic scale are used here.

A significant variation in magnitude of δ_{VSL} over the sphere surface is found at each Reynolds number (Figure 7), i.e., more than one order of magnitude. High values of δ_{VSL} correspond to low values of the shear stress at the wall (see Eq.(10)). The first peak in each curve (i.e. at $\theta > 80^\circ$) is located at the boundary-layer separation point ($\tau_w \ll \delta_{VSL} \gg$). The subsequent peaks also indicate locations within the recirculation zone in the wake of the sphere where a very low shear stress is found. Furthermore, a distinct decrease of $\delta_{VSL,avg}$ (i.e., increase of $d/\delta_{VSL,avg}$) with the Reynolds number could be found (Figure 8). A good approximation of this decrease was found by following power law: $\delta_{VSL,avg} = 0.318Re^{-0.71}$ ($R^2 = 0.9996$).

3.3.3 Convective transfer from surface

In this section, the impact of a reduced surface area for scalar transfer on the convective scalar exchange with the environment is investigated. For this purpose, different surface coverage ratios are evaluated ($\vartheta = 1\%, 5\%, 10\%, 20\%, 40\%, 60\%, 80\%, 100\%$) at multiple Reynolds numbers ($Re = 10-10^4$), hence covering a large d/δ_{VSL} range (see Figure 8). As mentioned in section 2.1, the discretely-distributed microscopic scalar sources are characterised by a constant scalar value ($T_w = 20^\circ\text{C}$), whereas the rest of the surface is assumed impermeable (no-flux condition), i.e. adiabatic. There will be some dependency of the resulting heat flow (and thus CHTC) on the specific distribution of the scalar sources over the surface, which was chosen randomly. The impact of the introduced randomness on the heat exchange is quantified by evaluating 10 different distributions at a low coverage ratios (10%) and at a high Reynolds number ($U_{ref} = 2 \text{ ms}^{-1}$) for a sphere. Due to the low coverage ratio and the large d/δ_{VSL} ratio (see Figure 6), the spread with varying coverage distribution, if significant, is expected to be relatively large here. However, a standard deviation of only 1% on the average heat flow of these 10 distributions is found, indicating a very small variation with coverage distribution. Due to this low sensitivity, only a single coverage distribution is evaluated for a specific coverage ratio in the remainder of this study.

474

475 In Figure 9, the surface-averaged heat flows ($Q_{c,w,avg}$) of the sphere are presented as a function of the surface
 476 coverage ratio (ϑ), for different $d/\delta_{VSL,avg}$ ratios, thus Reynolds numbers. These heat flows are scaled with the
 477 surface-averaged heat flow of a coverage ratio of 100% ($Q_{c,w,avg,100\%}$). The corresponding flow ratio from the
 478 analytical expression of Schlünder (1988) (Eq.(8), Figure 6b) is also included for several $d/\delta_{VSL,avg}$ ratios. Note
 479 that the CFD simulation results cover both the turbulent and laminar flow regime. Similar (scaled) surface-
 480 averaged heat flows are presented in Figure 10 for the apple at a Reynolds number of 10^4 ($U_{ref} = 2 \text{ ms}^{-1}$), i.e.,
 481 at a $d/\delta_{VSL,avg}$ ratio of 0.64. From Figure 9 and 10, relatively high heat flows at the surface are found at quite
 482 low coverage ratios (for all $d/\delta_{VSL,avg}$ ratios), which is similar to the findings of Schlünder (1988) for laminar
 483 flow over a flat plate. At a specific $d/\delta_{VSL,avg}$ ratio however, Schlünder found a more pronounced effect of low
 484 coverage ratios on the scalar transfer from the surface. This is not related to the absence of turbulence since
 485 the laminar flow cases in the present study also deviate from Schlünder's findings. Most probably, this
 486 difference is related to the boundary-layer behaviour: (1) For the flat plate of Schlünder (1988), the boundary
 487 layer is under equilibrium conditions and was developed whereas on the sphere surface, the boundary layer is
 488 still strongly developing and its profile is much more complex, e.g in recirculation zones or around separation
 489 and stagnation points; (2) In this study, heat transfer and shear stress are not correlated (see Figure 5). A more
 490 detailed and fundamental fluid mechanics study on the specific transport processes in the boundary layer,
 491 combining both experiments and numerical simulations, could shed more light here, but was out of the scope
 492 of this study. Consequently, it is probably not appropriate to compare heat exchange based on the (surface-
 493 averaged) $d/\delta_{VSL,avg}$ ratios (Figure 9) of this study with those of Schlünder. Note that the heat flow from the
 494 apple, as a function of coverage ratio, is very similar to that of the sphere (Figure 10).

495

496 Furthermore, at a specific coverage ratio, Schlünder (1988) always found higher scalar flows for decreasing
 497 $d/\delta_{VSL,avg}$ ratios, i.e., decreasing Reynolds numbers. In the present study, this effect is also present, except at
 498 the lowest Reynolds number ($Re = 10$, $U_{ref} = 0.002 \text{ ms}^{-1}$). Here, lower heat flows are actually found, at a
 499 specific coverage ratio, than for the subsequent Reynolds number ($Re = 100$, $U_{ref} = 0.02 \text{ ms}^{-1}$), for almost the
 500 entire range of evaluated coverage ratios. This discrepancy with Schlünder's findings is attributed to the fact

that the flow field (recirculation length, separation angle, turbulence, etc.) around the sphere significantly changes within the lowest Reynolds number range. These changes in the flow field will affect the total scalar transfer from the surface and can counteract to some extent the higher scalar flows at low Reynolds numbers as found by Schlünder. For Figure 9 and 10, it should be kept in mind that there is actually some uncertainty on the curves due to the randomness of the chosen distribution (as discussed earlier in this section). This uncertainty is, however, much smaller (standard deviation of about 1%) than the differences between the different Reynolds numbers ($d/\delta_{VSL,avg}$ ratios) at a specific coverage ratio. In the next paragraph, a more local assessment of scalar transfer along the sphere surface is presented.

In Figure 11, the distribution of local heat fluxes at the sphere surface is given as a function of the angle from the windward stagnation point for different surface coverage ratios at a Reynolds number of 10^4 ($U_{ref} = 2 \text{ ms}^{-1}$). The surface-averaged values over one-degree intervals (i.e., sphere segments) are represented. Note, however, that these surface-averaged heat fluxes of the sphere segments (SS) only average over the computational cells which are microscopic scalar sources, and not account for the remainder impermeable (adiabatic) part of the surface (thus using $A_{eff,SS}$ instead of A_{SS}). Thereby, in particular at low coverage ratios, no heat fluxes are reported (i.e., not shown in Figure 11: the curve is interrupted here) for some angles (sphere segments) since the local coverage ratio is zero. Two types of scaling are applied in Figure 11: (1) in Figure 11a, the segment-averaged heat flux of the sphere segments at a specific coverage ratio ($q_{c,w,SS,g}$) is scaled with the surface-averaged heat flux of the entire sphere for a coverage ratio of 100% ($q_{c,w,avg,100\%}$); (2) in Figure 11b, the segment-averaged heat flux of the sphere segment at a specific coverage ratio ($q_{c,w,SS,g}$) is scaled with the average heat flux of that sphere segment for a coverage ratio of 100% ($q_{c,w,SS,100\%}$). In Figure 11b, $\delta_{VSL}/\delta_{VSL,avg}$ is also included.

Figure 11a indicates that the local heat fluxes at the scalar sources increase with decreasing coverage ratio everywhere at the sphere surface, i.e., within each sphere segment. Low coverage ratios thus enhance the scalar exchange (heat fluxes) at these sources, as the boundary layer surrounding these sources is at a lower temperature, allowing for higher local transfer rates. Figure 11b represents the difference, locally (for each

sphere segment of 1°), of a partially-covered surface with an entirely covered surface, where for each sphere segment also the enhancement of the scalar exchange (heat fluxes) with decreasing coverage ratio is shown, compared to a coverage ratio of 100%, for which $q_{c,w,SS,\theta}/q_{c,w,SS,100\%} = 1$. Two distinct peaks can be noticed for each coverage ratio, namely around 90° and 125° . These peaks roughly correspond to the peaks in $\delta_{VSL}/\delta_{VSL,avg}$ (see also Figure 7). The largest differences between $q_{c,w,SS,\theta}$ and $q_{c,w,SS,100\%}$ are thus predominantly found near locations with high δ_{VSL} values (i.e., low d/δ_{VSL} values). This finding corresponds to the previous findings of Schlünder (1988) and of Figure 9: at low d/δ_{VSL} ratios ($d/\delta_{VSL,avg}$ in Figure 9), the relative heat flow from the surface at partial coverage was the largest. In Figure 11b, this finding is indicated in a local manner, i.e., for sphere segments. Note, however, that this finding does not hold at every location on the surface, e.g., at the windward stagnation point, where high δ_{VSL} values give low $q_{c,w,SS,\theta}/q_{c,w,SS,100\%}$ ratios. This is due to the bad correlation between the shear stress and the heat flux here (see Figure 5), where in the region between 90° - 125° , a rather good correlation is obtained. Although the shear stress, and derived quantities (δ_{VSL}), are appropriate for analysis of scalar transfer for flat plates (e.g., Schlünder, 1988), they seem less suitable for flow around complex geometries.

3.3.4 Definition of CHTCs

Convective heat transfer is usually quantified by means of C(H)TCs in numerical modelling. Note, however, that Eqs.(6-7) define the CTCs instead of specifying them as known information on the wall boundary (Lienhard and Lienhard, 2006). The choice of the used surface area (A or A_{eff}) in Eqs.(6-7) becomes a critical component in this definition for the discretely-distributed scalar sources investigated in section 3.3. Usually, the total surface area is used ($CHTC = Q_{c,w,avg}/(A(T_w - T_{ref}))$), by which the CHTC decreases with decreasing coverage ratio as shown in Figure 12a, as it is directly proportional to the heat flow (see Figure 9). Note, however, that this decrease is not linearly proportional with the coverage ratio.

Another option is to define the CTCs by only considering the discrete sources where the actual scalar exchange occurs. This implies that only the surface area of these discrete sources, i.e., the covered area (A_{eff}),

is accounted for in the definition of the CTCs ($\text{CHTC}_{\text{eff}} = Q_{c,w,\text{avg}}/(A_{\text{eff}}(T_w - T_{\text{ref}}))$). Using this CTC definition, a CTC increase is observed for the sphere with decreasing coverage ratio, as shown in Figure 12b. The reason for this is that the heat flux at the discrete sources increases significantly as the coverage ratio decreases (see Figure 11).

In conclusion of section 3.3, there is a clear impact of partial coverage of the surface on the resulting scalar exchange and CTCs, where relatively high scalar exchange rates can still be found at low coverage ratios. A complex dependency on the coverage ratio (θ), the Reynolds number (δ_{VSL}) and the size of the sources (d) is found, however. Note that the size of the sources was not varied explicitly in this study, but its influence was accounted for by varying the Reynolds number, thus the d/δ_{VSL} ratio.

4. Discussion

This paper deals with convective transfer predictions for horticultural products. Accurate modelling of the air-side convective transfer is, however, not always critical, namely when the scalar transport within the product dominates the kinetics of the scalar exchange with the environment: for many horticultural products, the resistance to moisture transfer of the inner tissue but especially of the cuticle (i.e., cuticle and wax layer for apple) and epidermis is much larger than the boundary-layer resistance (e.g., Nguyen et al., 2006). In this case, accurate modelling of the CMTC will not significantly improve convective mass exchange predictions. A similar remark can be made regarding convective heat exchange, but here the difference between boundary-layer and product-tissue resistances is usually smaller. The CMTC becomes particularly relevant at low air speeds (high boundary-layer resistance), for low cuticle resistances (e.g., for peach fruit, Lescourret et al., 2001; Morandi et al., 2010) or near protrusions in the cuticle (e.g., lenticels or cracks, Harker and Ferguson, 1988; Dietz et al., 1988; Veraverbeke et al., 2003a). Note that for droplet evaporation from surfaces of horticultural products, the exchange rate is always dominated by the air-side transfer (CMTC), by which accurate knowledge of CMTCs, but also CHTCs, is required. Also note that in this study, convective transfer of a single scalar was considered. In reality however, convective mass exchange, e.g. from evaporation of droplets, is actually coupled to some extent to convective heat transfer and vice versa, due to the (saturation)

vapour pressure and the latent heat of vaporisation. For low evaporation rates, a quasi-isothermal state will be induced, by which this coupling is quite weak and both transfer mechanisms can be considered quasi uncoupled.

Although only air-side scalar transfer was considered in this study, the convective transfer (and thus the CTC) is always to some extent coupled to the heat and/or mass transport within the product, and is determined by the complex energy (and mass) balance at the product surface, which often changes over time (transient conditions). Consequently, the commonly applied boundary conditions over the product surface (e.g., uniform scalar or flux) to predict CTCs for these products are actually simplifications of reality. For more accurate modelling, a conjugate approach should be used, where the relevant transport processes in both the air and the product are solved simultaneously. Recently, Defraeye et al. (2012) showed that using a conjugate approach could clearly increase CTC accuracy in some cases, whereas in other cases, no significant increase in accuracy was found. The sensitivity of CTC predictions to conjugate modelling was rather low for cases where the resistance to transfer within the material (i.e., the product) was relatively high, compared to that of the boundary layer. Since this is the case in this study (as mentioned in previous paragraph), the applied boundary conditions are likely to be representative here, but further research with conjugate modelling is required, and ongoing. Conjugate modelling of coupled heat and mass transport in the air combined with fruit tissue however remains very challenging, to date.

In contrast to previous studies, which applied homogeneous boundary conditions to quantify scalar transfer from horticultural products, the scalar exchange in this study was also modelled using heterogeneous boundary conditions, namely discretely-distributed microscopic scalar sources. Such discrete modelling required a very high grid resolution on the product surface (thus also in the boundary layer, due to LRNM), which is often not practically feasible for complex flow systems due to the high computational expense (e.g., in stacks of products, Kondjoyan, 2006): in such studies, the computational cells on the surface of the horticultural product typically have a hydraulic diameter of about 10^{-2} m, i.e., at a macroscopic scale, whereas 10^{-4} m was required in this study. In order to incorporate the effect of discrete sources in such complex flow

systems, a multiscale modelling approach could be more appropriate: empirically-determined functions could be used in the macroscopic continuum model to relate the scalar flow rate of each computational cell ($\sim 10^{-2}$ m) or, on average, of the entire product to the coverage ratio of the surface, the Reynolds number and the size of the scalar sources. Due to the spatial dependency of this flow rate over the product surface for a specific coverage ratio (see section 3.3), these functions will be quite complex and are probably rather difficult to generalise.

It was shown in this study that applying CTCs obtained from well-established convective transfer research on spheres with homogeneous (macroscopic) boundary conditions (100% coverage ratio) can result in a significant overprediction of the convective exchange, compared to the actual heterogeneous boundary conditions (microscopic scalar sources). This effect is especially manifested at low surface coverage ratios, such as for lenticels or surface cracks, where the coverage ratio is around, e.g., 1% and 10%, respectively, for apple fruit (Veraverbeke et al., 2003a). Based on the present study, the CMTC of a spherical product with lenticels or cracks will then be about 10%-40% (for lenticels) and 50%-80% (for cracks) of that of a sphere with a coverage ratio of 100% (see Figure 9), depending on the Reynolds number. Such a mismatch between CMTCs for fully-covered and partially-covered conditions can strongly compromise the accuracy of convective exchange predictions in several pre- and postharvest applications.

The obtained CHTCs in this study were derived to be representative for CMTCs by quasi satisfying the similarity criteria for the analogy, amongst others, by imposing similar boundary conditions. In many cases, these similarity criteria cannot be (entirely) satisfied, by which the analogy cannot be strictly applied. In addition, the uniform boundary conditions which are usually applied to determine the CTCs are generally not found in reality, which can affect the surface-averaged CTCs and the CTC distribution over the surface. These aspects will be addressed in a follow-up study.

The drag, Nusselt number, recirculation length and separation angle of the apple agreed quite well with that of a sphere. In reality, however, some variability on these values will be found for horticultural products due to

Defraeye T., Herremans E., Verboven P., Carmeliet J., Nicolai B. (2012), Convective heat and mass exchange at surfaces of horticultural products: a microscale CFD modelling approach, *Agricultural and Forest Meteorology* 162-163, 71-84. <http://dx.doi.org/10.1016/j.agrformet.2012.04.010>
<http://www.journals.elsevier.com/agricultural-and-forest-meteorology/>

the evaluated species, the cultivar, the unique shape of each individual product, the Reynolds number, the orientation to the approach flow, the turbulence characteristics of the approach flow, surface roughness of the product and the specific configuration (e.g., products in a stack). Such variability will be addressed in a follow-up study.

Due to the generic configuration that is considered in this study (i.e., a sphere), the findings are also useful in other fields of research dealing with convective transfer at surfaces of spherical objects, e.g., in chemical engineering (e.g., packed beds, Dixon et al., 2011) or with scalar transfer/reactions at discretely-distributed locations at the air-material interface, e.g., for drying of porous materials (Schlünder, 1988; Belhamri and Fohr, 1996; Defraeye et al., 2012).

Finally, it is important to clearly state the assumptions made in this numerical study, in order to allow a proper interpretation of the presented results and to indicate points for further refinement of the model in the future. Following assumptions are made: (1) Since the focus was on passive scalar transport in this study, only forced convection was considered and buoyancy was not modelled; (2) Since the focus was on general convective scalar transport, thus also towards an applicability for mass transfer, the influence of radiation was not taken into account in the model; (3) For similar reasons, no coupling between heat and mass transfer was accounted for, and only heat transfer was considered; (4) Due to the use of LRNM for modelling the transport in the boundary layer, surface roughness could not be accounted for. Surface roughness can however enhance scalar transfer rates and can alter the flow field around the product; (5) To reduce the complexity of the computational model, the thickness (hence volume) of microscopic scalar sources, such as droplets, was not considered; (6) To allow comparison with previous studies on spheres and to provide a well-conditioned air flow, the product was placed in a virtual wind-tunnel environment, implying low turbulence levels. These flow conditions however differ from those of the natural environment of a horticultural product, e.g. in an orchard or greenhouse. The aim of this study was however, amongst others, to indicate the performance, accuracy and applicability of CFD for this type of studies to other researchers. CFD has certainly proven to be

a valuable tool to assess convective transfer from horticultural products, also at the microscale, and can be used consequently to study transfer from products in more realistic environments.

5. Conclusions

Convective passive scalar exchange at surfaces of horticultural products was investigated in this study by means of CFD. A single product was considered with heat as the acting scalar. A sphere was used as a reference system and a typical horticultural product (i.e., an apple) was considered as a model system. CFD validation of the fluid flow and scalar transfer was performed for the sphere. A very good performance of the RANS SST k- ω turbulence model was found regarding drag coefficient, Nusselt number, separation angle and recirculation length for a large Reynolds number range ($10 - 3 \times 10^4$). The drag, flow field and scalar transfer of a sphere and a typical apple compared well over this Reynolds number range, indicating that a sphere can be used as an approximation for spherically-shaped horticultural products. Furthermore, the impact of a reduced surface area for scalar transfer on the convective scalar exchange with the environment was investigated. For heterogeneous boundary conditions on the product surface (i.e., discretely-distributed microscopic scalar sources such as lenticels or droplets), the scalar flow from the surface did not scale linearly with the surface coverage ratio. Instead, relatively large flow rates (and thus C(H)TCs) were found, even if scalar flow occurs only at a fraction of the surface area of the horticultural product (very low coverage ratios), due to the increase of the local fluxes at these sources with decreasing coverage ratio. The magnitude of these flow rates was dependent on the coverage ratio, the Reynolds number and the size of the sources. This paper raises an important aspect in CTC predictions for horticultural products by means of CFD or wind-tunnel research: although discrete modelling of these microscopic scalar sources is required in some cases to obtain more accurate CTCs, instead of applying continuum modelling with homogeneous, uniform boundary conditions, it is often not practically feasible (computationally or experimentally) for complex geometries (e.g., stack of spheres) due to the small scale of these sources. For such configurations, a multiscale modelling approach is more realistic, which will be the focus of future research. Note however that performing a similar

Defraeye T., Herremans E., Verboven P., Carmeliet J., Nicolai B. (2012), Convective heat and mass exchange at surfaces of horticultural products: a microscale CFD modelling approach, *Agricultural and Forest Meteorology* 162-163, 71-84. <http://dx.doi.org/10.1016/j.agrformet.2012.04.010>
<http://www.journals.elsevier.com/agricultural-and-forest-meteorology/>

experimental study on an entire horticultural product, comparable to the numerical study presented here, would be very difficult, due to the small (microscopic) scales involved, clearly indicating the benefits of the numerical approach used here. Although this study focussed on microscale modelling of horticultural products, the obtained results are certainly valuable for studies on similar effects with other plant organs, such as the effect of stomata on moisture exchange of leaves with the environment.

Acknowledgements

Thijs Defraeye is a postdoctoral fellow of the Research Foundation – Flanders (FWO). Els Herremans acknowledges IWT Flanders for financial support. Financial support by the Research Foundation – Flanders (project FWO G.0603.08) and K.U.Leuven (project OT 08/023) is also gratefully acknowledged. These sponsors had no involvement in: the study design, the collection, analysis and interpretation of data; the writing of the manuscript; and the decision to submit the manuscript for publication.

Defraeye T., Herremans E., Verboven P., Carmeliet J., Nicolai B. (2012), Convective heat and mass exchange at surfaces of horticultural products: a microscale CFD modelling approach, *Agricultural and Forest Meteorology* 162-163, 71-84. <http://dx.doi.org/10.1016/j.agrformet.2012.04.010>
<http://www.journals.elsevier.com/agricultural-and-forest-meteorology/>

References

- Abdul Majeed, P.M., 1981. Analysis of heat transfer during hydrair cooling of spherical food products. *Int. J. Heat Mass Tran.* 24(2), 323-333.
- Acevedo, C., Sanchez, E., Young, M.E., 2007. Heat and mass transfer coefficients for natural convection in fruit packages. *J. Food Eng.* 80(2), 655-661.
- Allais, I., Alvarez, G., Flick, D., 2006. Modelling cooling kinetics of a stack of spheres during mist chilling. *J. Food Eng.* 72(2), 197-209.
- Alvarez, G., Flick, D., 1999. Analysis of heterogeneous cooling of agricultural products inside bins Part II: thermal study. *J. Food Eng.* 39(3), 239-245.
- Ambaw, A., Beaudry, R., Bulens, I., Delele, M.A., Ho, Q.T., Schenk, A., Nicolai, B., Verboven, P., 2011. Modeling the diffusion-adsorption kinetics of 1-methylcyclopropene (1-MCP) in apple fruit and non-target materials in storage rooms. *J Food Eng.* 102(3), 257-265.
- Augier, F., Idoux, F., Delenne, J.Y., 2010. Numerical simulations of transfer and transport properties inside packed beds of spherical particles. *Chem. Eng. Sci.* 65(3), 1055-1064.
- Barati, E., Esfahani, J.A., 2011. A new solution approach for simultaneous heat and mass transfer during convective drying of mango. *J. Food Eng.* 102(4), 302-309.
- Belhamri, A., Fohr, J.P., 1996. Heat and mass transfer along a wetted porous plate in an airstream. *AIChE J.* 42(7), 1833-1843.
- Boehncke, A., Siebers, J., Nolting, H.-G., 1990. Investigations of the evaporation of selected pesticides from natural and model surfaces in field and laboratory. *Chemosphere* 21(9), 1109-1124.
- Casey, M., Wintergerste, T., 2000. ERCOFTAC Special Interest Group on "Quality and Trust in Industrial CFD": Best Practice Guidelines, ERCOFTAC.
- Cebeci, T., Bradshaw, P., 1984. *Physical and Computational aspects of Convective Heat Transfer*. first ed. Springer-Verlag New York Inc., USA.
- Chilton, T.H., Colburn, A.P., 1934. Mass transfer (absorption) coefficients. *Ind. Eng. Chem.* 26(11), 1183-1187.

Defraeye T., Herremans E., Verboven P., Carmeliet J., Nicolai B. (2012), Convective heat and mass exchange at surfaces of horticultural products: a microscale CFD modelling approach, *Agricultural and Forest Meteorology* 162-163, 71-84. <http://dx.doi.org/10.1016/j.agrformet.2012.04.010>
<http://www.journals.elsevier.com/agricultural-and-forest-meteorology/>

- 725 Clift, R., Grace, J.R., Weber, M.E., 1978. Bubbles, drops and particles. first ed. Dover Publications Inc., New
 726 York, USA.
- 727 Constantinescu, G., Squires, K., 2004. Numerical investigations of flow over a sphere in the subcritical and
 728 supercritical regimes. *Phys. Fluids* 16(5), 1449-1466.
- 729 Constantinescu, G., Chapelet, M., Squires, K., 2003. Turbulence modelling applied to flow over a sphere.
 730 *AIAA J.* 41(9), 1733- 1742.
- 731 Cross, J.V., Walklate, P.J., Murray, R.A., Richardson, G.M., 2001. Spray deposits and losses in different sized
 732 apple trees from an axial fan orchard sprayer: 2. Effects of spray quality. *Crop Prot.* 20(4), 333-343.
- 733 da Silva, W.P., e Silva, C.M.D.P.S., Farias, O.V.S., e Silva, D.D.P.S., 2010. Calculation of the convective
 734 heat transfer coefficient and cooling kinetics of an individual fig fruit. *Heat Mass Transfer* 46(3), 371-380.
- 735 Datta, A.K., 2007a. Porous media approaches to studying simultaneous heat and mass transfer in food
 736 processes. I: Problem formulations. *J. Food Eng.* 80(1), 80-95.
- 737 Datta, A.K., 2007b. Porous media approaches to studying simultaneous heat and mass transfer in food
 738 processes. II: Property data and representative results. *J. Food Eng.* 80(1), 96-110.
- 739 Defraeye, T., Blocken, B., Carmeliet, J., 2010a. CFD analysis of convective heat transfer at the surfaces of a
 740 cube immersed in a turbulent boundary layer. *Int. J. Heat Mass Tran.* 53(1-3), 297-308.
- 741 Defraeye, T., Blocken, B., Koninckx, E., Hespel, P., Carmeliet, J., 2010b. Computational fluid dynamics
 742 analysis of cyclist aerodynamics: Performance of different turbulence-modelling and boundary-layer
 743 modelling approaches. *J. Biomech.* 43(12), 2281-2287.
- 744 Defraeye, T., Blocken, B., Carmeliet, J., 2012. Analysis of convective heat and mass transfer coefficients for
 745 convective drying of a porous flat plate by conjugate modelling. *Int. J. Heat Mass Tran.* 55(1-3), 112-124.
- 746 Dehghannya, J., Ngadi, M., Vigneault, C., 2010. Mathematical modeling procedures for airflow, heat and
 747 mass transfer during forced convection cooling of produce: A review. *Food Eng. Rev.* 2(4), 227-243.
- 748 Delele, M., Tijssens, E., Atalay, Y.T., Ho, Q.T., Ramon, H., Nicolai, B., Verboven, P., 2008. Combined
 749 discrete element and CFD modelling of airflow through random stacking of horticultural products in
 750 vented boxes. *J. Food Eng.* 89(1), 33-41.

Defraeye T., Herremans E., Verboven P., Carmeliet J., Nicolai B. (2012), Convective heat and mass exchange at surfaces of horticultural products: a microscale CFD modelling approach, *Agricultural and Forest Meteorology* 162-163, 71-84. <http://dx.doi.org/10.1016/j.agrformet.2012.04.010>
<http://www.journals.elsevier.com/agricultural-and-forest-meteorology/>

- 751 Delele, M., Schenk, A., Tijssens, E., Ramon, H., Nicolai, B., Verboven, P., 2009. Optimization of the
 752 humidification of cold stores by pressurized water atomizers based on a multiscale CFD model. *J. Food*
 753 *Eng.*, 91(2), 228-239.
- 754 Dhole, S.D., Chhabra, R.P., Eswaran, V., 2006. A numerical study on the forced convection heat transfer from
 755 an isothermal and isoflux sphere in the steady symmetric flow regime. *Int. J. Heat Mass Tran.* 49(5-6),
 756 984-994.
- 757 Dietz, T.H., Thimma Raju, K.R., Joshi, S.S., 1988. Studies on loss of weight of mango fruits as influenced by
 758 cuticles and lenticels. *Acta Horticulturae* 231, 685-687.
- 759 Dixon, A.G., Taskin, M.E., Nijemeisland, M., Stitt, E.H., 2011. Systematic mesh development for 3D CFD
 760 simulation of fixed beds: Single sphere study. *Comp. Chem. Eng.* 35(7), 1171-1185.
- 761 Ebert, T.A., Downer, R.A., 2006. A different look at experiments on pesticide distribution. *Crop Prot.* 25(4),
 762 299-309.
- 763 Everett, K.R., Hallett, I.C., Rees-George, J., Chynoweth, R.W., Pak, H.A., 2008. Avocado lenticel damage:
 764 The cause and the effect on fruit quality. *Postharvest Biol. Tec.* 48(3), 383-390.
- 765 Feng, Z.G., Michaelides, E.E., 2000. A numerical study on the transient heat transfer from a sphere at high
 766 Reynolds and Peclet numbers. *Int. J. Heat Mass Tran.* 43(2), 219-229.
- 767 Ferrua, M.J., Singh, R.P., 2009. Modeling the forced-air cooling process of fresh strawberry packages, Part I:
 768 Numerical model. *Int. J. Refrig.* 32(2), 335-348.
- 769 Ferrua, M.J., Singh, R.P., 2011. Improved airflow method and packaging system for forced-air cooling of
 770 strawberries. *Int. J. Refrig.* 34(4), 1162-1173.
- 771 Ferziger, J.H., Peric, M., 2002. Computational methods for Fluid Dynamics. third ed. Springer-Verlag Berlin
 772 Heidelberg New York, Germany.
- 773 Fluent 12, 2009. Ansys Fluent 12.0 User's Guide. Ansys Inc.
- 774 Franke, J., Hellsten, A., Schlünzen, H., Carissimo, B., 2007. Best practice guideline for the CFD simulation of
 775 flows in the urban environment, COST Action 732: Quality assurance and improvement of microscale
 776 meteorological models, Hamburg, Germany.

Defraeye T., Herremans E., Verboven P., Carmeliet J., Nicolai B. (2012), Convective heat and mass exchange at surfaces of horticultural products: a microscale CFD modelling approach, *Agricultural and Forest Meteorology* 162-163, 71-84. <http://dx.doi.org/10.1016/j.agrformet.2012.04.010>
<http://www.journals.elsevier.com/agricultural-and-forest-meteorology/>

- 777 Galloway, T.R., Sage, B.H., 1972. Local and macroscopic thermal transport from a sphere in a turbulent air
 778 stream. *AIChE J.* 18(2), 287-293.
- 779 Ghisalberti, L., Kondjoyan, A., 1999. Convective heat transfer coefficients between air flow and a short
 780 cylinder. Effect of air velocity and turbulence. Effect of body shape, dimensions and position in the flow. *J.*
 781 *Food Eng.* 42(1), 33-44.
- 782 Harker, F.R., Ferguson, I.B., 1988. Transport of calcium across cuticles isolated from apple fruit. *Sci. Hortic.*
 783 36(3-4), 205-217.
- 784 Ho, Q.T., Verboven, P., Verlinden, B., Lammertyn, J., Vandewalle, S., Nicolai, B., 2008. A continuum model
 785 for metabolic gas exchange in pear fruit. *PLoS Comp. Biol.* 4(3), art.nr. e1000023.
- 786 Ho, Q.T., Verboven, P., Verlinden, B., Herremans, E., Wevers, M., Carmeliet, J., Nicolai, B., 2011. A 3-D
 787 multiscale model for gas exchange in fruit. *Plant Physiol.* 155(3), 1158-1168.
- 788 Hoang, M.L., Verboven, P., Baelmans, M., Nicolai, B., 2004. Sensitivity of temperature and weight loss in the
 789 bulk of chicory roots with respect to process and product parameters. *J. Food Eng.* 62(3), 233-243.
- 790 Hu, Z., Sun, D.-W., 2001. Predicting the local surface heat transfer coefficients by different turbulent k- ϵ
 791 models to simulate heat and moisture transfer during air-blast chilling. *Int. J. Refrig.* 24(7), 702-717.
- 792 Johnson, T.A., Patel, V.C., 1999. Flow past a sphere up to a Reynolds number of 300. *J. Fluid Mech.* 378, 19-
 793 70.
- 794 Jones, H.G., Higgs, K.H., 1982. Surface conductance and water balance of developing apple (*Malus pumila*
 795 Mill.) fruits. *J. Exp. Bot.* 33(132), 67-77.
- 796 Kaya, A., Aydin, O., Dincer, I., 2006. Numerical modeling of heat and mass transfer during forced convection
 797 drying of rectangular moist objects. *Int. J. Heat Mass Tran.* 49(17-18), 3094-3103.
- 798 Kondjoyan, A., 2006. A review on surface heat and mass transfer coefficients during air chilling and storage
 799 of food products. *Int. J. Refrig.* 29(6), 863-875.
- 800 Kovacs, E., Kovacs, J., Zackel, E., Genova, J., 1994. Structural and chemical changes of pear skin. *Acta*
 801 *Horticulturae* 368, 243-250.
- 802 Krokida, M.K., Maroulis, Z.B., Marinos-Kouris, D., 2002. Heat and mass transfer coefficients in drying:
 803 compilation of literature data. *Dry. Technol.* 20(1), 1-18.

Defraeye T., Herremans E., Verboven P., Carmeliet J., Nicolai B. (2012), Convective heat and mass exchange at surfaces of horticultural products: a microscale CFD modelling approach, *Agricultural and Forest Meteorology* 162-163, 71-84. <http://dx.doi.org/10.1016/j.agrformet.2012.04.010>
<http://www.journals.elsevier.com/agricultural-and-forest-meteorology/>

- 804 Lammertyn, J., Scheerlinck, N., Jancsó, P., Verlinden, B.E., Nicolai, B., 2003a. A respiration-diffusion
805 model for ‘Conference’ pears I: model development and validation. *Postharvest Biol. Tec.* 30(1), 29-42.
- 806 Lammertyn, J., Scheerlinck, N., Jancsó, P., Verlinden, B.E., Nicolai, B., 2003b. A respiration-diffusion
807 model for ‘Conference’ pears II. Simulations and relation to core breakdown. *Postharvest Biol. Tec.* 30(1),
808 43-55.
- 809 Lamnatou, Chr., Papanicolaou, E., Belessiotis, V., Kyriakis, N., 2009. Conjugate heat and mass transfer from
810 a drying rectangular cylinder in confined air flow. *Numer. Heat Tr. A- Appl.* 56(5), 379-405.
- 811 Lamnatou, Chr., Papanicolaou, E., Belessiotis, V., Kyriakis, N., 2010. Finite-volume modelling of heat and
812 mass transfer during convective drying of porous bodies - Non-conjugate and conjugate formulations
813 involving the aerodynamic effects. *Renew. Energ.* 35(7), 1391-1402.
- 814 Launder, B.E., 1988. On the computation of convective heat transfer in complex turbulent flows. *J. Heat*
815 *Trans. - T. ASME* 110, 1112-1128.
- 816 Launder, B.E., Spalding, D.B., 1974. The numerical computation of turbulent flows. *Comp. Meth. Appl. M.*
817 3(2), 269-289.
- 818 Leca, A., Parisi, L., Lacointe, A., Saudreau, M., 2011. Comparison of Penman–Monteith and non-linear
819 energy balance approaches for estimating leaf wetness duration and apple scab infection. *Agr. Forest*
820 *Meteorol.* 151(8), 1158-1162.
- 821 Lescourret, F., Génard, M., Habib, R., Fishman, S., 2001, Variation in surface conductance to water vapor
822 diffusion in peach fruit and its effects on fruit growth assessed by a simulation model. *Tree Physiol.* 21,
823 735-741.
- 824 Lienhard IV, J.H., Lienhard V, J.H., 2006. A Heat Transfer Textbook. Third ed. Phlogiston Press, Cambridge
825 Massachusetts, USA.
- 826 Majdoubi, H., Boulard, T., Fatnassi, H., Bouirden, L., 2009. Airflow and microclimate patterns in a one-
827 hectare Canary type greenhouse: An experimental and CFD assisted study. *Agr. Forest Meteorol.* 149(6-7),
828 1050-1062
- 829 Martins, M.A., Oliveira, L.S., Saraz, J.A., 2011. Numerical study of apple cooling in tandem arrangement.
830 *Dyna-Colombia*, 78(166), 158-165.

Defraeye T., Herremans E., Verboven P., Carmeliet J., Nicolai B. (2012), Convective heat and mass exchange at surfaces of horticultural products: a microscale CFD modelling approach, *Agricultural and Forest Meteorology* 162-163, 71-84. <http://dx.doi.org/10.1016/j.agrformet.2012.04.010>
<http://www.journals.elsevier.com/agricultural-and-forest-meteorology/>

- 831 McMinn, W.A.M., Magee, T.R.A., 1999. Principles, methods and applications of the convective drying of
832 foodstuffs. *Food Bioprod. Process.* 77(3), 175-193.
- 833 Melese Endalew, A., Debaer, C., Rutten, N., Vercammen, J., Delele, M.A., Ramon, H., Nicolai, B., Verboven,
834 P., 2010. Modelling pesticide flow and deposition from air-assisted orchard spraying in orchards: A new
835 integrated CFD approach. *Agr. Forest Meteorol.* 150(10), 1383-1392.
- 836 Menter, F.R., 1994. Two-equation eddy-viscosity turbulence models for engineering applications. *AIAA J.*
837 32(8), 1598-1605.
- 838 Morandi, B., Manfrini, L., Losciale, P., Zibordi, M., Corelli-Grappadelli, L., 2010. The positive effect of skin
839 transpiration in peach fruit growth. *J. Plant Physiol.* 167(13), 1033-1037.
- 840 Mujumdar, A.S., Law, C.L., 2010. Drying technology: trends and applications in postharvest processing. *Food*
841 *Bioprocess Tech.* 3(6), 843-852.
- 842 Nahor, H., Hoang, M., Verboven, P., Baelmans, M., Nicolai, B., 2005. CFD model of the airflow, heat and
843 mass transfer in cool stores. *Int. J. Refrig* 28(3), 368-380.
- 844 Nguyen, T., Verboven, P., Schenk, A., Nicolai, B., 2007. Prediction of water loss from pears (*Pyrus*
845 *communis* cv. Conference) during controlled atmosphere storage as affected by relative humidity. *J. Food*
846 *Eng.* 83(2), 149-155.
- 847 Nguyen, T.A., Dresselaers, T., Verboven, P., D'hallewin, G., Culeddu, N., Van Hecke, P., Nicolai, B., 2006.
848 Finite element modelling and MRI validation of 3D transient water profiles in pears during postharvest
849 storage. *J. Sci. Food Agr.* 86(5), 745-756.
- 850 Peyrin, F., Kondjoyan, A., 2002. Effect of turbulent integral length scale on heat transfer around a circular
851 cylinder placed cross to an air flow. *Exp. Therm. Fluid Sci.* 26(5), 455-460.
- 852 Roache, P.J., 1994. Perspective: a method for uniform reporting of grid refinement studies. *J. Fluid Eng. - T.*
853 *ASME* 116(3), 405-413.
- 854 Saudreau, M., Sinoquet, H., Santin, O., Marquier, A., Adam, B., Longuenesse, J.-J., Guilioni, L., Chelle, M.,
855 2007. A 3D model for simulating the spatial and temporal distribution of temperature within ellipsoidal
856 fruit. *Agr. Forest Meteorol.* 147(1-2), 1-15.

Defraeye T., Herremans E., Verboven P., Carmeliet J., Nicolai B. (2012), Convective heat and mass exchange at surfaces of horticultural products: a microscale CFD modelling approach, *Agricultural and Forest Meteorology* 162-163, 71-84. <http://dx.doi.org/10.1016/j.agrformet.2012.04.010>
<http://www.journals.elsevier.com/agricultural-and-forest-meteorology/>

- 857 Schlünder, E.U., 1988. On the mechanism of the constant drying rate period and its relevance to diffusion
858 controlled catalytic gas phase reactions. *Chem. Eng. Sci.* 43(10), 2685-2688.
- 859 Schlünder, E.U., 2004. Drying of porous material during the constant and the falling rate period: A critical
860 review of existing hypotheses. *Dry. Technol.* 22(6), 1517-1532.
- 861 Sekse, L., 1995. Fruit cracking in sweet cherries (*Prunus avium* L.). Some physiological aspects - a mini
862 review. *Sci. Hortic.* 63(3-4), 135-141.
- 863 Suzuki, M., Maeda, S., 1968. On the mechanism of drying of granular beds. *J. Chem. Eng. Jpn.* 1(1), 26-31.
- 864 Tashtoush, B., 2000. Natural losses from vegetable and fruit products in cold storage. *Food Control* 11(6),
865 465-470.
- 866 Tutar, M., Erdogdu, F., Toka, B., 2009. Computational modeling of airflow patterns and heat transfer
867 prediction through stacked layers' products in a vented box during cooling. *Int. J. Refrig.* 32(2), 295-306.
- 868 Veraverbeke, E.A., Verboven, P., Van Oostveldt, P., Nicolai, B., 2003a. Prediction of moisture loss across the
869 cuticle of apple (*Malus sylvestris* subsp. *mitis* (Wallr.)) during storage: Part 1. Model development and
870 determination of diffusion coefficients. *Postharvest Biol. Tec.* 30(1), 75-88.
- 871 Veraverbeke, E.A., Verboven, P., Van Oostveldt, P., Nicolai, B., 2003b. Prediction of moisture loss across the
872 cuticle of apple (*Malus sylvestris* subsp. *mitis* (Wallr.)) during storage: Part 2. Model simulations and
873 practical applications. *Postharvest Biol. Tec.* 30(1), 89-97.
- 874 Verboven, P., Flick, D., Nicolai, B., Alvarez, G., 2006. Modelling transport phenomena in refrigerated food
875 bulks, packages and stacks: basics and advances. *Int. J. Refrig.* 29(6), 985-997.
- 876 Verboven, P., Datta, A.K., Anh, N.T., Scheerlinck, N., Nicolai, B., 2003. Computation of airflow effects on
877 heat and mass transfer in a microwave oven. *J. Food Eng.* 59(2-3), 181-190.
- 878 Verboven, P., Nicolai, B., Scheerlinck, N., De Baerdemaeker, J., 1997. The local surface heat transfer
879 coefficient in thermal food process calculations: a CFD approach. *J. Food Eng.* 33(1-2), 15-35.
- 880 Whitaker, S., 1972. Forced convection heat transfer correlations for flow in pipes, past flat plates, single
881 cylinders, single spheres, and for flow in packed beds and tube bundles. *Am. Inst. Chem. Eng. J.* 18(2),
882 361-371.

Defraeye T., Herremans E., Verboven P., Carmeliet J., Nicolai B. (2012), Convective heat and mass exchange at surfaces of horticultural products: a microscale CFD modelling approach, *Agricultural and Forest Meteorology* 162-163, 71-84. <http://dx.doi.org/10.1016/j.agrformet.2012.04.010>
<http://www.journals.elsevier.com/agricultural-and-forest-meteorology/>

- 883 Xu, L., Zhu, H., Ozkan, H.E., Thistle, H.W., 2010. Evaporation rate and development of wetted area of water
884 droplets with and without surfactant at different locations on waxy leaf surfaces. *Biosyst. Eng.* 106 (1), 58-
885 67.
- 886 Yu, Y., Zhu, H., Frantz, J.M., Reding, M.E., Chan, K.C., Ozkan, H.E., 2009. Evaporation and coverage area
887 of pesticide droplets on hairy and waxy leaves. *Biosyst. Eng.* 104 (3), 324-334.
- 888 Zou, Q., Opara, L.U., McKibbin, R., 2006. A CFD modeling system for airflow and heat transfer in ventilated
889 packaging for fresh foods: I. Initial analysis and development of mathematical models. *J. Food Eng.* 77(4),
890 1037-1047.
- 891
- 892

Figure captions

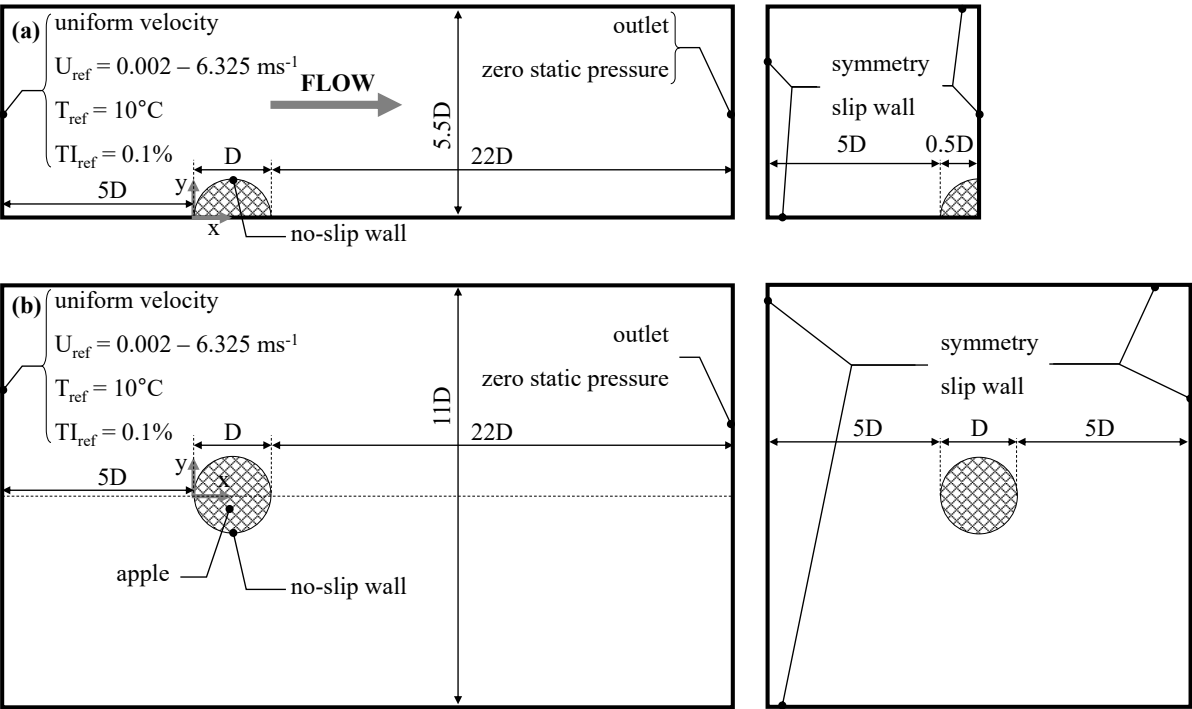


Figure 1. Computational domain (not to scale) and boundary conditions for: (a) sphere model, (b) apple fruit model (left: side view; right: frontal view). The apple is represented by a sphere in this figure.

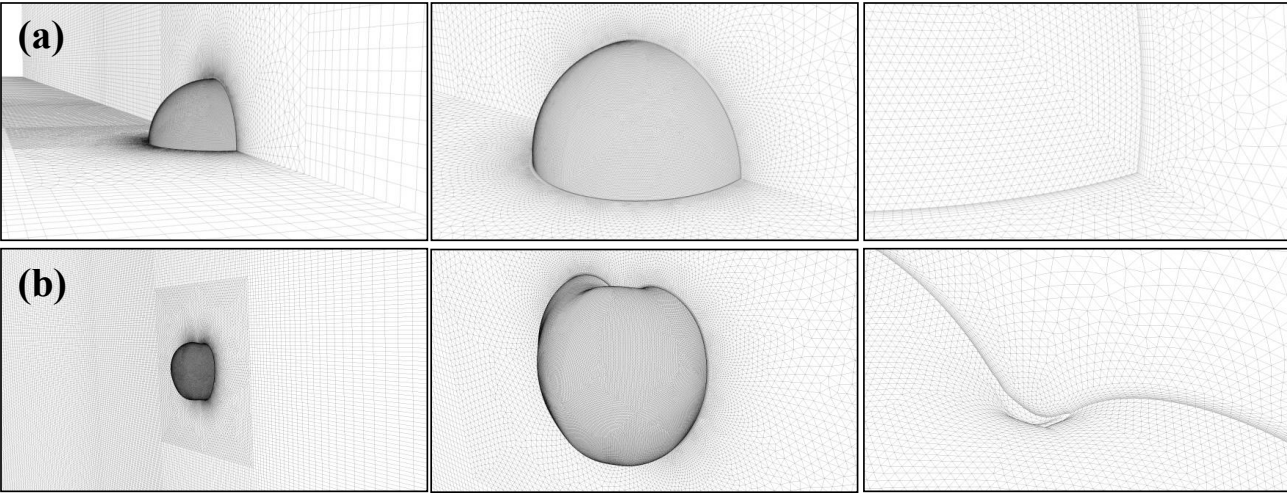


Figure 2. Computational grid for: (a) sphere model (1/4 sphere), (b) apple fruit model (entire fruit). The grid in a centreplane through the apple is shown.

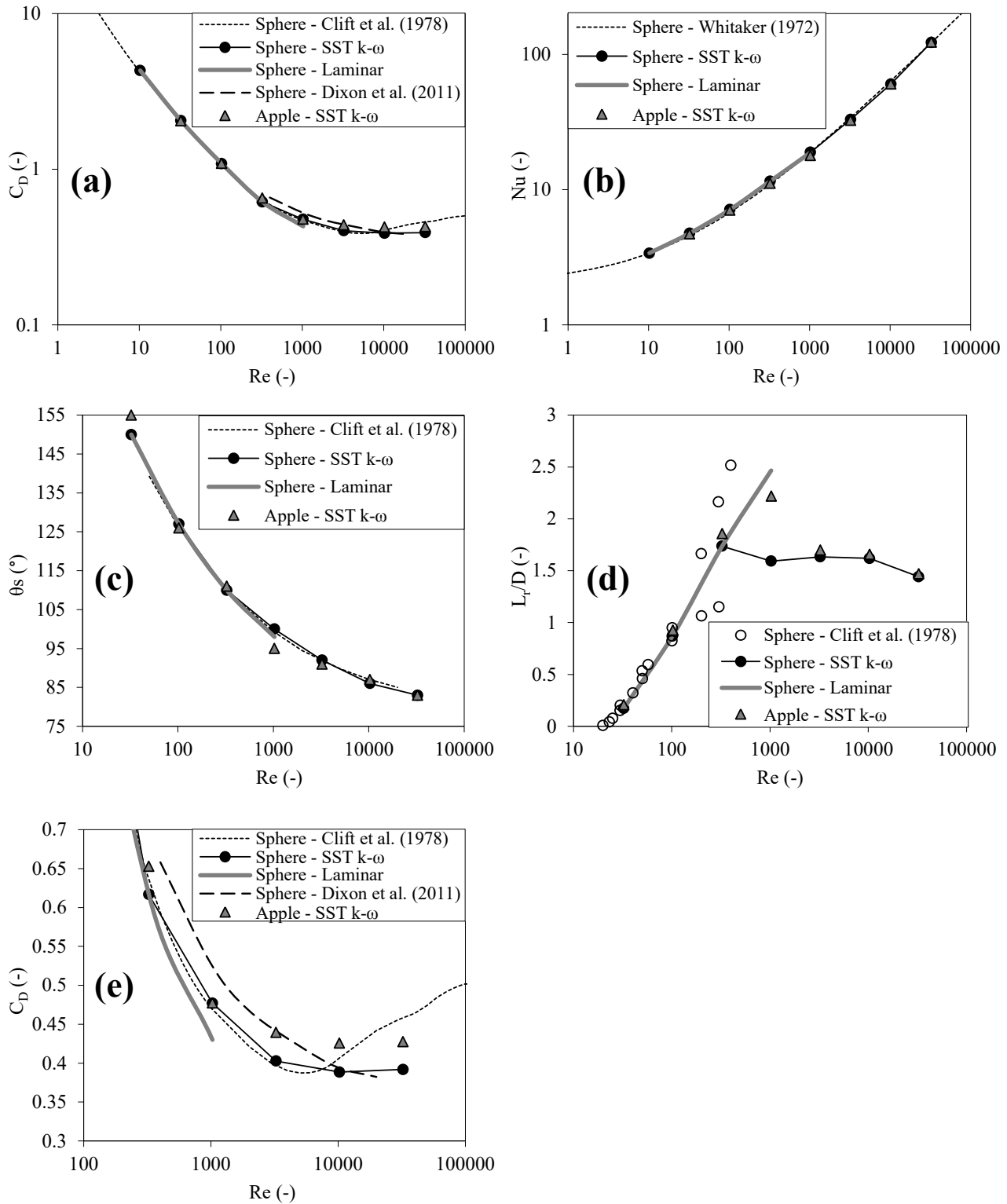
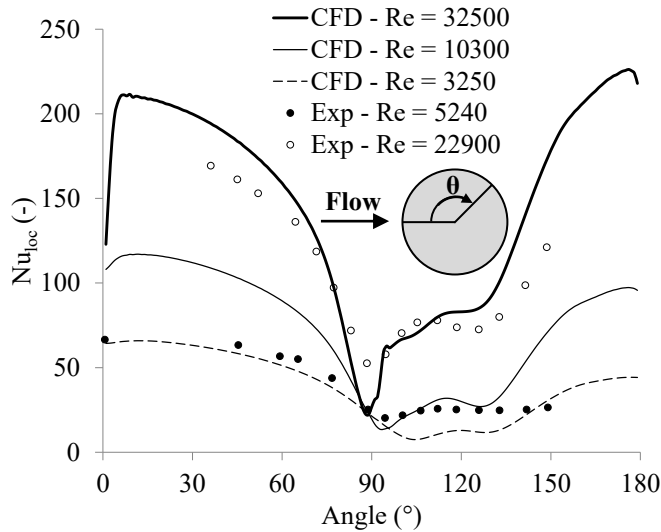


Figure 3. Comparison of CFD simulation data of a sphere (SST k- ω model and laminar model) and an apple (SST k- ω model) with empirical sphere data and numerical data of Dixon et al. (2011), as a function of Reynolds

904 number (logarithmic scale): (a) drag coefficient; (b) Nusselt number; (c) separation angle; (d) recirculation length,
 905 scaled with the sphere or (equivalent) apple diameter.



906
 907 **Figure 4. Comparison of CFD simulation data of a sphere (SST k- ω model) with empirical sphere data (Exp) of**
 908 **Galloway and Sage (1972) for the local Nusselt number as a function of the angle (θ , zero at windward stagnation**
 909 **point) for different Reynolds numbers.**

910

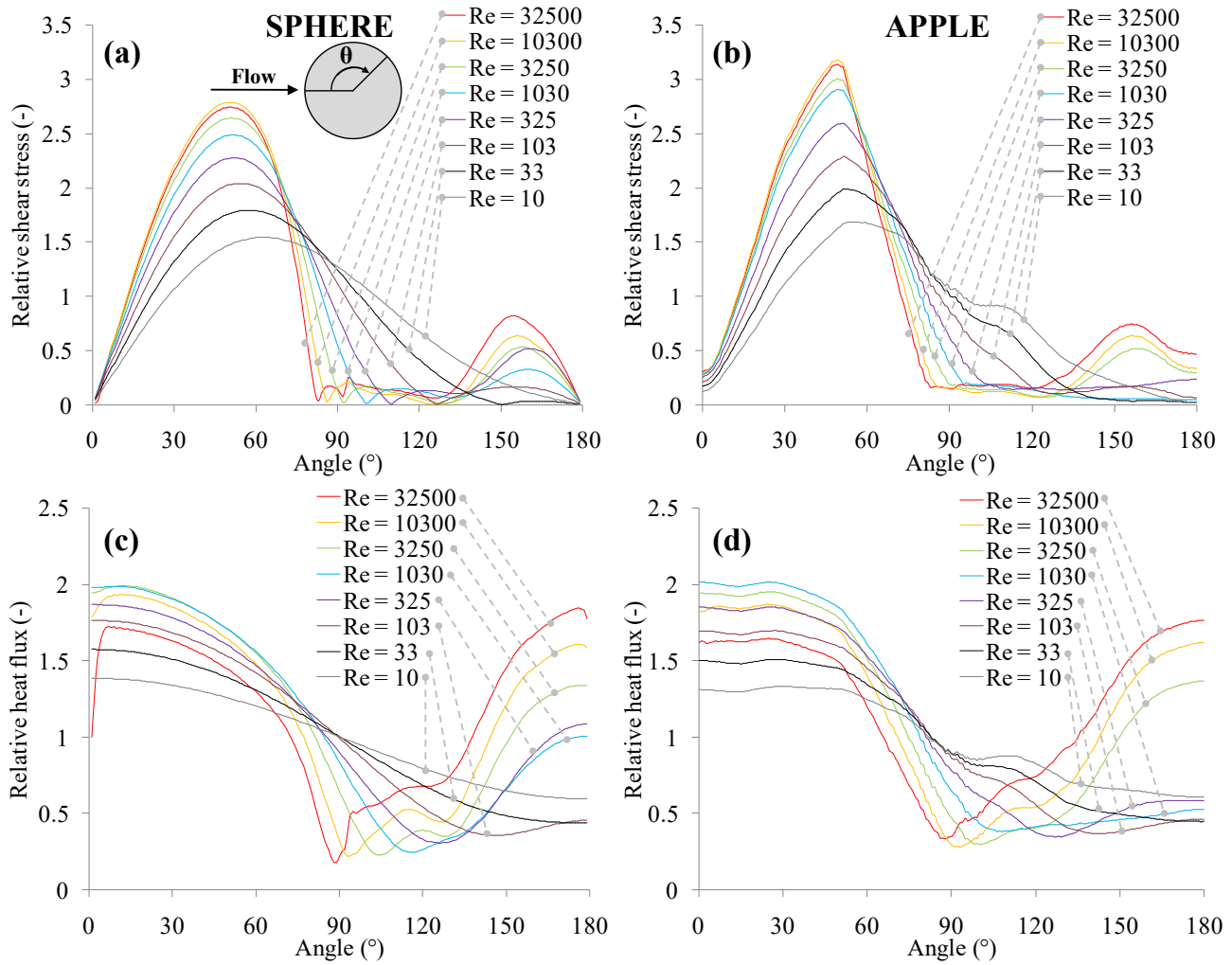


Figure 5. Shear stress ((a) and (b)) and heat flux ((c) and (d)) for a sphere and an apple as a function of the angle (θ , zero at windward stagnation point) at different Reynolds numbers (SST $k-\omega$ model). Both parameters are scaled with the surface-averaged values over the sphere or apple.

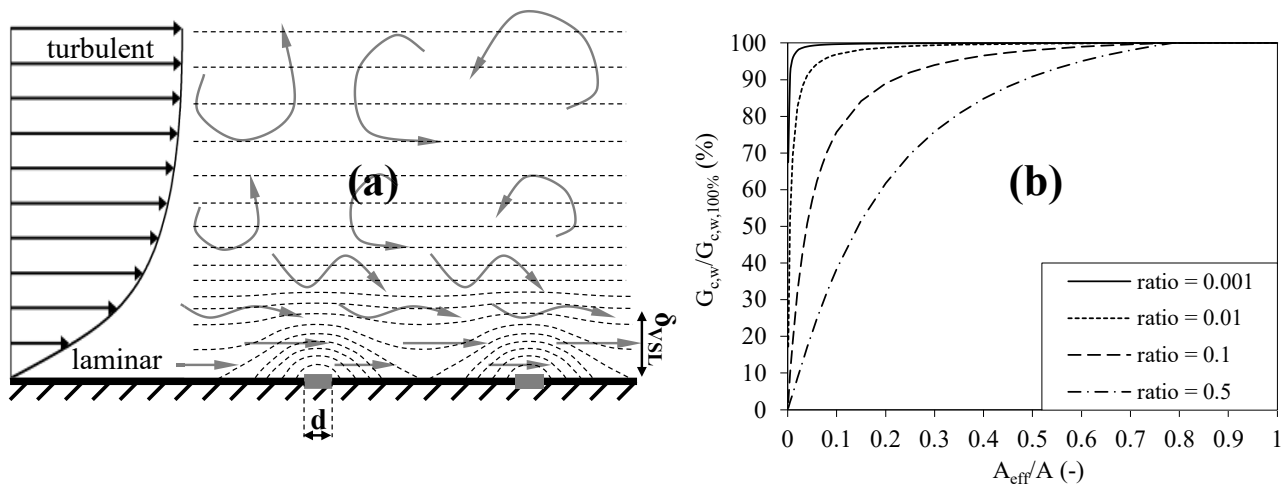


Figure 6. (a) Scalar (concentration) contours in the boundary layer over a wall surface with discretely-distributed patches (i.e., moisture sources, indicated in grey) with indication of d and δ_{VSL} and also laminar and turbulent regions in the boundary layer; (b) Mass flow rate as a function of the surface coverage ratio ($\vartheta = A_{eff}/A$) according to Eq.(8) from Schlünder (1988) for different d/δ_{VSL} ratios. The mass flow rate of the surface is scaled with that of a surface with a coverage ratio of 100%.

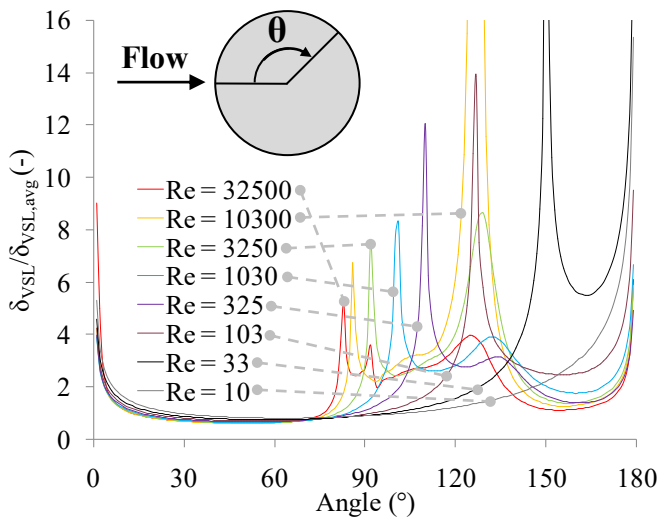


Figure 7. Viscous boundary-layer thickness for a sphere as a function of the angle (θ , zero at windward stagnation point) at different Reynolds numbers (SST k- ω model). This boundary-layer thickness is scaled with the surface-averaged value over the sphere.

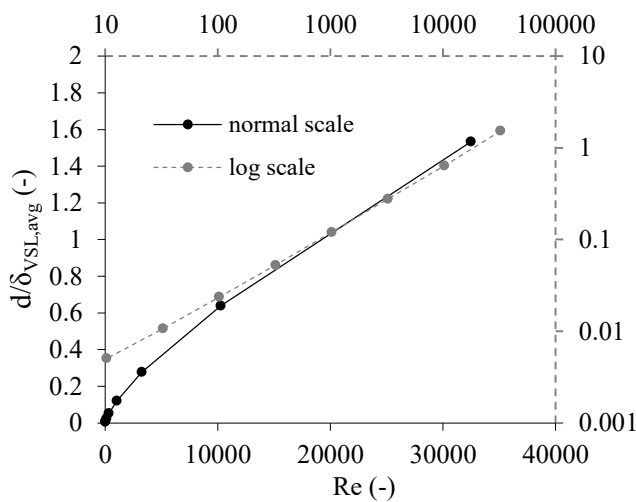


Figure 8. Surface-averaged $d/\delta_{VSL,avg}$ ratios of a sphere as a function of the Reynolds number. Both normal and logarithmic scaling are used.

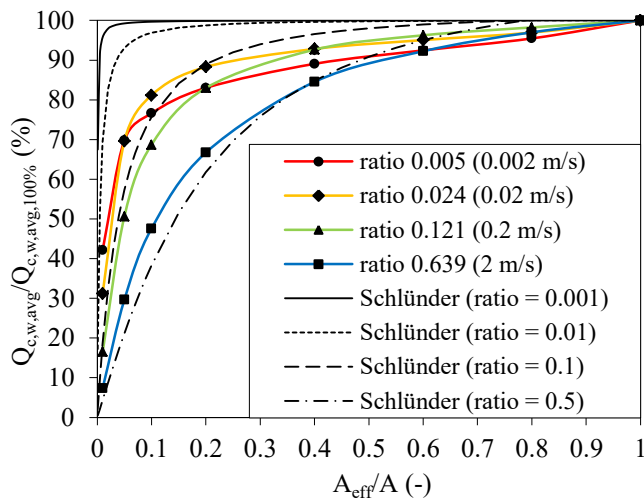


Figure 9. Surface-averaged heat flows of a sphere as a function of the surface coverage ratio ($g = A_{eff}/A$) for different d/δ_{VSL} ratios (i.e., air speeds U_{ref} via Eq. (10)) for CFD simulations and the ratio of Eq.(8) (Schlünder, 1988). The heat flow is scaled with that of a surface with a coverage ratio of 100%.

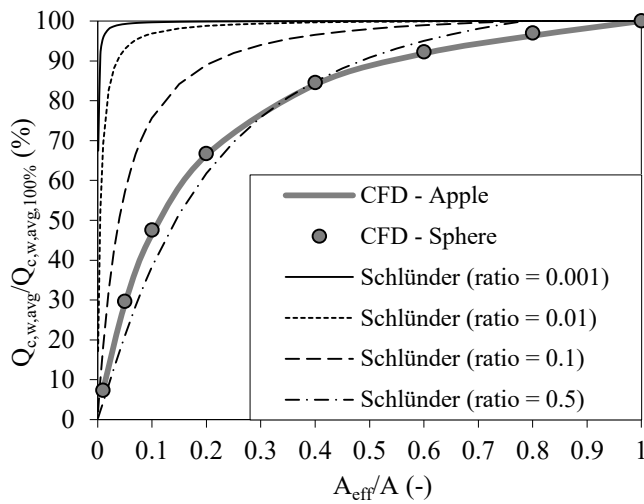


Figure 10. Surface-averaged heat flow of an apple and a sphere as a function of the surface coverage ratio ($g = A_{eff}/A$) for a d/δ_{VSL} ratio of 0.64 (i.e., an air speed $U_{ref} = 2 \text{ ms}^{-1}$) for CFD simulations and the ratio of Eq.(8) (Schlünder, 1988). The heat flow is scaled with that of a surface with a coverage ratio of 100%.

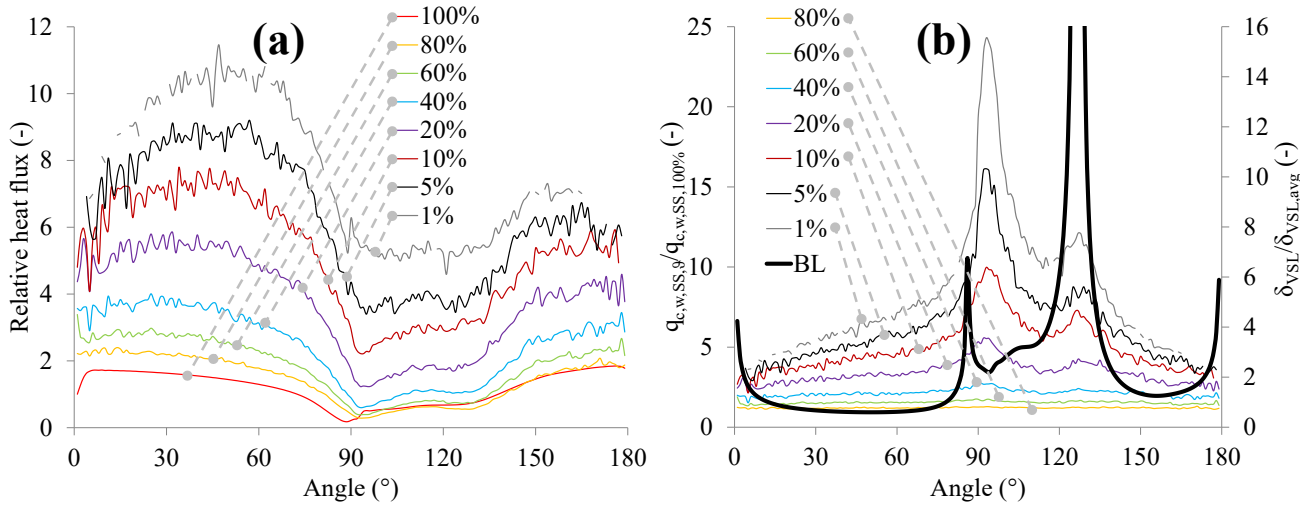


Figure 11. Heat flux for a sphere as a function of the angle (θ , zero at windward stagnation point) at a Reynolds number of 10^4 (SST $k-\omega$ model) for different surface coverage ratios (1% to 100%): (a) the heat flux is scaled with the surface-averaged value over the sphere for a coverage ratio of 100% ($q_{c,w,avg,100\%}$); (b) the heat flux is scaled with the local heat flux of that sphere segment of 1° for a coverage ratio of 100% ($q_{c,w,SS,100\%}$) and BL (boundary layer) indicates the $\delta_{VSL}/\delta_{VSL,avg}$ ratio, as in Figure 7.

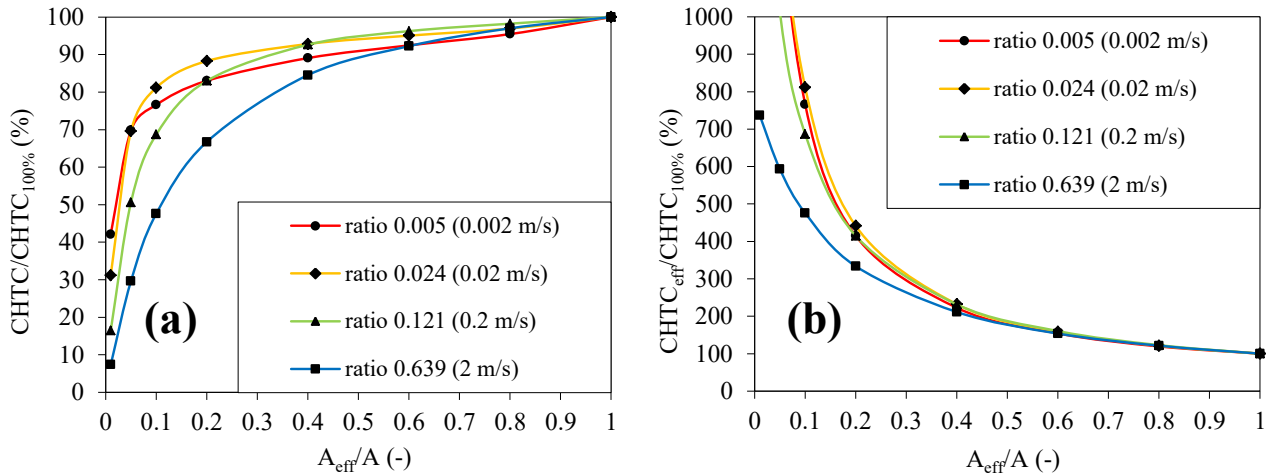


Figure 12. Surface-averaged CHTC of a sphere as a function of the surface coverage ratio ($g = A_{eff}/A$) for different d/δ_{VSL} ratios (i.e., air speeds U_{ref}) for the CFD simulations: (a) CHTC defined based on total surface area (A); (b) CHTC defined based on effective surface area (A_{eff}). The CHTCs are scaled with those of a sphere with a coverage ratio of 100%.

Defraeye T., Herremans E., Verboven P., Carmeliet J., Nicolai B. (2012), Convective heat and mass exchange at surfaces of horticultural products: a microscale CFD modelling approach, *Agricultural and Forest Meteorology* 162-163, 71-84. <http://dx.doi.org/10.1016/j.agrformet.2012.04.010>
<http://www.journals.elsevier.com/agricultural-and-forest-meteorology/>

Tables

Table 1. Surface-averaged heat flux ($q_{c,w,avg}$) and shear stress ($\tau_{w,avg}$) for sphere and apple (used in Figure 5) for different Reynolds numbers.

Reynolds number	Wind speed (ms ⁻¹)	Sphere		Apple	
		$\tau_{w,avg}$ (Pa)	$q_{c,w,avg}$ (Wm ⁻²)	$\tau_{w,avg}$ (Pa)	$q_{c,w,avg}$ (Wm ⁻²)
10	0.002	2.01 x 10 ⁻⁶	10.9	1.94 x 10 ⁻⁶	10.7
33	0.006325	9.00 x 10 ⁻⁶	15.3	8.71 x 10 ⁻⁶	15.0
103	0.02	4.40 x 10 ⁻⁵	23.0	4.27 x 10 ⁻⁵	22.4
325	0.06325	2.18 x 10 ⁻⁴	37.3	2.12 x 10 ⁻⁴	35.5
1030	0.2	1.14 x 10 ⁻³	60.9	1.05 x 10 ⁻³	57.0
3250	0.6325	6.05 x 10 ⁻³	106.7	5.82 x 10 ⁻³	103.8
10300	2	3.21 x 10 ⁻²	195.0	3.11 x 10 ⁻²	192.8
32500	6.325	1.85 x 10 ⁻¹	395.3	1.80 x 10 ⁻¹	391.9